

# Efficiency of Short-Pulse Type-I Second-Harmonic Generation With Simultaneous Spatial Walk-Off, Temporal Walk-Off, and Pump Depletion

Haifeng Wang and Andrew M. Weiner, *Fellow, IEEE*

**Abstract**—We have developed a theory which for the first time predicts the efficiency of type-I second-harmonic generation (SHG) with simultaneous spatial and temporal walk-offs and with pump depletion. In order to validate our theory, we have compared its predictions with a numerical solver. We also have measured the conversion efficiency for type-I SHG in experiments with  $\sim 120$ -fs laser pulses in BBO and LBO crystals long enough that both temporal and spatial walk-off are important. Comparison supports our theoretical analysis. Our theory provides a useful tool for estimating SHG efficiency with pulsed sources in both nondepletion and depletion regions.

**Index Terms**—Femtosecond pulses, nonlinear optics, second-harmonic generation (SHG).

## I. INTRODUCTION

SECOND-HARMONIC generation (SHG), also known as frequency doubling, is an important nonlinear optical process which was first demonstrated shortly after the invention of the laser [1]. SHG provides a simple way to generate coherent light at wavelengths near 400 nm or below, which is attractive to numerous applications including optical data storage, optical printing, visual displays, photolithography, and medical uses. It is also widely used for measurement of ultrafast optical pulses via autocorrelation [2] or frequency-resolved optical gating [3]. High conversion efficiency is always preferred if it does not significantly degrade other parameters. As a second-order process, there are two major ways to increase SHG efficiency for a specified nonlinear material: increase input intensity and increase crystal length. The former invokes the need for pulsed laser sources and beam focusing; the latter increases the significance of temporal and spatial walk-off effects, which are caused by group velocity mismatch (GVM) and birefringence, respectively. The walk-off effects can reshape the output light significantly if the crystal is long enough. The effect of spatial walk-off and focusing on the conversion efficiency and output field profile were already studied carefully for CW sources in a series of papers in the 1960s [4]–[7]. The effect of GVM and temporal walk-off for pulsed plane-wave

sources was also studied in early papers [8]–[11]; its effect on autocorrelation measurements of ultrashort pulses [12] and on pulse shaping using quasi-phase-matched gratings [13] has also been analyzed.

Despite four decades of experience with SHG, calculation of SHG efficiency via analytical methods is rather involved even for type-I processes unless significant simplifying assumptions are made. A classic paper written by Boyd and Kleinman [7] carefully investigated SHG with a CW laser in the case of no source depletion (low efficiency). Equation (2.99) in their paper gives simple formulas for the conversion efficiency valid for different parameter regions (e.g., strong versus weak focusing, strong versus weak spatial walk-off). This is very helpful for estimating efficiency and understanding the physics in CW SHG. However, as short pulse lasers replace CW lasers in much of nonlinear optics research, the two basic assumptions of [7] (CW source and low efficiency) are generally no longer true. As a result, there is a need for a theory which can handle focusing as well as temporal walk-off and which retains validity into the pump depletion region. One recent paper worked out the focusing dependence of type-I SHG with short pulse sources with large temporal walk-off, but without spatial walk-off and without pump depletion [14]. Here we present a theory which for the first time can give meaningful analytical predictions of type-I SHG efficiency for short pulse sources with simultaneous focusing, spatial walk-off, and temporal walk-off. Within the nondepleted pump approximation, our theory may be considered as an extension of [7] to include both space and time coordinates. However, our theory is valid not only for a nondepleted pump as in [7], but is also approximately valid well into the depleted pump regime.

In order to validate our theory, we performed experiments in which we measured the SHG efficiency in two nonlinear crystals (BBO and LBO) under different focusing conditions and different input powers. The experiments are performed under conditions when both spatial and temporal walk-off are important and with a conversion efficiency as high as 60%.

We have also compared the results of our theory with a numerical model which can treat the SHG process. Numerical models only need basic differential equations to work in many cases, can give very accurate results, and can be very versatile. Analytical models always have some limitations because, for a complicated process, approximations have to be made to derive an understandable analytical result. However, analytical models

Manuscript received April 29, 2003; revised August 27, 2003. This work was supported by the National Science Foundation under Grant 99000369-ECS and Grant 0100949-ECS.

The authors are with the School of Electrical and Computer Engineering, Purdue University, West Lafayette, IN 47907-1285 USA (e-mail: wangh@ecn.purdue.edu).

Digital Object Identifier 10.1109/JQE.2003.819531

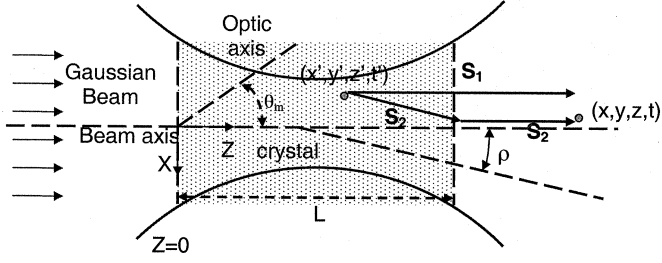


Fig. 1. A simple picture of SHG in nonlinear crystals.  $\mathbf{S}_1$ , and  $\mathbf{S}_2$  are the pointing vectors of the fundamental and harmonic fields, respectively.

have the advantage of providing greater insight, revealing the relationship between the parameters and predicting scaling rules.

The remainder of this paper is structured as follows. Our theory of pulsed sources with no depletion is discussed in Section II. Section III extends the theory to the depletion region. Section IV discusses how to evaluate the efficiency numerically using the theoretical equations and shows some calculated results. Section V compares the results of theoretical models (ours and Boyd and Kleinman's [7]) with those of the nonlinear optics solver SNLO from Sandia National Laboratories [15], [16]. Experimental results are presented and compared with the theory in Section V. Section VI presents the conclusion.

## II. SHG THEORY WITH PULSED INPUT AND NO SOURCE DEPLETION

As shown in Fig. 1, we assume an ooe type-I SHG process (although we expect the final results to work also for an eeo process) with only one input. The nonlinear crystal has length  $L$ , and its cross section is much larger than the input laser beam. We ignore any reflections at the crystal surfaces. The beam axis (which we term  $Z$ ) is normal to the crystal surface, and this is the direction of the input wavevector. The input surface of the crystal is at  $z = 0$ . The optic axis is taken to lie in the  $XZ$  plane.  $\theta_m$  is the phase-matching angle and  $\rho$  is the spatial walk-off angle between the input fundamental beam and the output second-harmonic (SH) beam. For ooe SHG, the polarization of the input field is taken along  $Y$ , and the output SH field is polarized along  $X$ . In this paper, we will write the fields in scalar form, since we have already assumed that they are linearly polarized and we know their field direction. We use MKS units.

In our theory, we consider group velocity mismatch (GVM) between fundamental and SH fields, but ignore the fundamental pulse broadening due to group velocity dispersion (GVD). This is justified in our experiments, in which we studied SHG of  $\sim 120$ -fs pulses in an 8-mm-long BBO crystal and in a 15-mm-long LBO crystal. In both cases, broadening of the fundamental pulse due to material dispersion is calculated to be only a few femtoseconds. If much shorter pulses were used for SHG, the effect of dispersion would eventually become important. We also neglect any material absorption in the nonlinear crystal.

The basic idea is that the SH field outside the crystal is the integral of the contributions from all the sources inside the crystal. We use  $(x', y', z', t')$  to represent a source point inside the crystal and  $(x, y, z, t)$  to represent an observer point as in Fig. 1. We write the fields inside the nonlinear crystal as the following:

$$E_1(x', y', z', t') = \frac{1}{2}(A_1(x', y', z', t')e^{i(\omega_1 t' - k_1 z')} + c.c.) \quad (1a)$$

$$E_2(x', y', z', t') = \frac{1}{2}(A_2(x', y', z', t')e^{i(\omega_2 t' - k_2 z')} + c.c.) \quad (1b)$$

$$P_{NL}(x', y', z', t') = \frac{1}{2}(P_2(x', y', z', t')e^{i2(\omega_1 t' - k_1 z')} + c.c.) \quad (1c)$$

Here we use  $\mathbf{E}$  to represent the total field and  $\mathbf{A}$  to represent the complex amplitude free of fast-oscillating terms.  $\omega_1$  is the center frequency of the fundamental wave, and  $k_1$  is the wavevector of the fundamental wave inside the crystal at  $\omega_1$ ;  $\omega_2 = 2\omega_1$  and  $k_2$  is the wavevector at  $\omega_2$ . For a CW source,  $\mathbf{A}_1$  is independent of  $t'$ . The fundamental field excites an SH polarization field in the nonlinear crystal

$$P_{NL}(x', y', z', t') = 2\varepsilon_0 d_{\text{eff}} E_1^2(x', y', z', t') \\ = \frac{\varepsilon_0 d_{\text{eff}}}{2} (A_1^2 e^{i2(\omega_1 t' - k_1 z')} + c.c.) \quad (2a)$$

$$P_2(x', y', z', t') = \varepsilon_0 d_{\text{eff}} A_1^2(x', y', z', t'). \quad (2b)$$

Equation (1c) and (2a) result in (2b). Considering a CW plane-wave source, it can be shown that the harmonic field amplitude at output end of the crystal ( $z = L$ ) is (see [5, eq. (3.7)]):

$$A_2(L) = -\frac{i\omega_2 \mu_0 c}{2n_2} \int_0^L P_2(z') \exp(i\Delta k z') dz' \\ = -i\kappa \int_0^L A_1^2(z') \exp(i\Delta k z') dz' \quad (3)$$

where  $\kappa = \omega_1 d_{\text{eff}} / n_2 c$  is the coupling coefficient;  $n_2$  is the refractive index of the SH wave and  $\Delta k = k_2 - 2k_1$  is the phase mismatch.

Equation (3) is valid for CW plane waves. For pulsed Gaussian beam input, things are much more complicated, and the formula for the harmonic field at the output end of the crystal [cf. (11)] is formally derived in the Appendix. However, here we use an approach, which we term the extended heuristic approach, to derive it. We present this approach because it is both straightforward and insightful.

In [6], a Green's function was derived for CW SHG by an arbitrary polarization; the total SH field was obtained by integrating this Green's function over a Gaussian beam. It was shown that the Green's function has the property that energy propagates from the source point to the observer point along the direction of the Poynting vector, as in Fig. 1. This means that, for a certain observer point, the source points that contribute

must lie on the same ray. This method, termed the heuristic approach in [7], allows us to set up a relationship between the spatial coordinates of source points and the observer point. Because in our case we use pulses instead of a CW source, we have an extra coordinate in the time domain. Therefore, here we extend the heuristic approach to include a short pulse source by assuming that energy propagates from the source point to the observer point both along the ray and at the group velocity. This is justified by comparing (11), derived here using the extended heuristic approach, with the formal results derived in the Appendix.

The heuristic approach results in

$$\begin{aligned} x' &= x - \rho(L - z') = x - \rho L + \rho z' \\ y' &= y \\ t' &= t - \frac{L - z'}{V_2}. \end{aligned} \quad (4)$$

Here we have assumed  $z = L$  (the observer point is right at the inner side of the end of the crystal).  $V_2$  is the group velocity of the SH wave. Expressions for  $V_2$ , as well as the group velocity of the fundamental wave ( $V_1$ ) and the group velocity mismatch (GVM), denoted as  $\beta$ , are given by

$$V_1 = \frac{\partial \omega}{\partial k_1} \quad V_2 = \frac{\partial \omega}{\partial k_2} \quad \beta = \frac{1}{V_2} - \frac{1}{V_1}. \quad (5)$$

Because the Poynting vector and the wavevector are in different directions for the SH wave,  $V_2$  is not the total energy-flow velocity, but is rather its  $Z$  component (in the wavevector direction).

Since (3) is valid for CW plane waves, it should also be valid for CW waves which are nearly plane waves except for being finite in the  $X$  and  $Y$  directions. To include the case that the source is pulsed but the waveform does not change in the whole process (ignoring GVD), we just add a temporal coordinate and relate the source points and the observer point with (4). By using the extended heuristic approach, we can extend (3) to obtain

$$\begin{aligned} A_2(x, y, L, t) &= -i\kappa \int_0^L A_1^2(x', y', z', t') \exp(i\Delta k z') dz' \\ &= -i\kappa \int_0^L A_1^2\left(x - \rho L + \rho z', y, z', t - \frac{L}{V_2} + \frac{z'}{V_2}\right) \\ &\quad \cdot \exp(i\Delta k z') dz'. \end{aligned} \quad (6)$$

Since a focused Gaussian beam is not a nearly plane wave, the field propagation from the source points to the observer point must be taken into account. However, based on (6), we can still write down the incremental harmonic field at the source point (before propagation) as

$$dA_2(x', y', z', t') = -i\kappa A_1^2(x', y', z', t') \exp(i\Delta k z') dz'. \quad (7)$$

By properly dealing with field propagation and using the heuristic approach, we will be able to derive  $dA_2(x, y, L, t)/dz'$  from  $dA_2(x', y', z', t')/dz'$  and get an integral for  $A_2(x, y, L, t)$ . How exactly it is done for Gaussian beam will be shown below.

We assume the fundamental field is Gaussian both spatially and temporally. The complex amplitude can be written as [17]

$$\begin{aligned} A_1(x', y', z', t') &= \frac{A_0}{\sqrt{(1 - i\tau_x(z'))(1 - i\tau_y(z'))}} \\ &\quad \cdot \exp\left(-\frac{x'^2}{w_{0x}^2(1 - i\tau_x(z'))}\right) \\ &\quad \cdot \exp\left(-\frac{y'^2}{w_{0y}^2(1 - i\tau_y(z'))}\right) \\ &\quad \cdot \exp\left(-\frac{2 \ln 2 \left(t' - \frac{z'}{V_1}\right)^2}{t_p^2}\right) \\ &\quad \cdot \exp\left(-i \frac{\alpha \ln 2 \left(t' - \frac{z'}{V_1}\right)^2}{2t_p^2}\right) \end{aligned} \quad (8a)$$

$$\tau_x(z') = \frac{2(z' - z_{0x})}{b_x} \quad (8b)$$

$$\tau_y(z') = \frac{2(z' - z_{0y})}{b_y}. \quad (8c)$$

Some explanations of the above equations are given here.

$A_0$  is a constant. The spatial part of (8a) represents an elliptical Gaussian beam where  $w_{0x}$  and  $w_{0y}$  are the radii of the beam waist in the  $X$  and  $Y$  directions, respectively, and where the positions of the beam waist for the  $X$  and  $Y$  directions are  $z_{0x}$  and  $z_{0y}$ , respectively. The confocal parameters of the Gaussian beam for  $X$  and  $Y$  directions, which describe how divergent the beam is, are written as  $b_x = 2\pi n_1 w_{0x}^2 / \lambda_0$  and  $b_y = 2\pi n_1 w_{0y}^2 / \lambda_0$ . We use  $n_1$  and  $n_2$  as the refractive indices of the fundamental and harmonic waves, respectively. In (8a),  $\tau_x(\cdot)$  and  $\tau_y(\cdot)$  are two functions defined in (8b) and (8c).

In the temporal part of (8a),  $t_p$  is the full-width at half-maximum (FWHM) duration of the pulse in terms of intensity. We assume that the input fundamental spectrum is Gaussian with a quadratic spectral phase:  $\exp(-\omega^2 t_0^2 / 4) \exp(i p \omega^2)$  ( $t_0$  and  $p$  are both constant). By Fourier transforming it into the time domain we will have the temporal part in (8a) with  $\alpha = 16p/t_0^2$  and  $t_p = (1 + \alpha^2)^{1/2} t_0$ . Obviously the phase term represents a linear chirp. The pulse has a time-bandwidth product  $\Delta\nu \Delta t$  which is  $(1 + \alpha^2)^{1/2}$  times greater than the time-bandwidth product of a chirp-free Gaussian pulse. Here we ignore higher order chirps. Since we ignore pulse broadening due to GVD as mentioned previously, for the case of no source depletion the pulse will propagate at its group velocity with a fixed temporal profile.

By using (7), we have the incremental harmonic amplitude at the source point

$$\begin{aligned} dA_2(x', y', z', t') &= \\ &\quad \frac{-i\kappa A_0^2 \exp(i\Delta k z')}{\sqrt{(1 - i\tau_x(z'))(1 - i\tau_y(z'))}} \exp\left(-\frac{(4 + i\alpha) \ln 2 \left(t' - \frac{z'}{V_1}\right)^2}{t_p^2}\right) \\ &\quad \cdot \left\{ \frac{1}{\sqrt{(1 - i\tau_x(z'))(1 - i\tau_y(z'))}} \exp\left(-\frac{2x'^2}{w_{0x}^2(1 - i\tau_x(z'))}\right) \right. \\ &\quad \left. \cdot \exp\left(-\frac{2y'^2}{w_{0y}^2(1 - i\tau_y(z'))}\right) \right\} dz'. \end{aligned} \quad (9)$$

To deal with field propagation we need to notice that the part enclosed in the brackets has the form of the amplitude of a Gaussian beam of spot size  $w_{0x}/\sqrt{2}$  and  $w_{0y}/\sqrt{2}$ , confocal parameter  $b_x$  and  $b_y$ , and beam waist position  $z_{0x}$  and  $z_{0y}$ . It is this part which propagates, because it is known as a solution of the wave equation in the paraxial approximation. To propagate from  $(x', y', z', t')$  to  $(x, y, L, t)$ , we replace  $\tau_x(z')$ ,  $\tau_y(z')$  by  $\tau_x(L)$ ,  $\tau_y(L)$  in the brackets and use the extended heuristic approach [(4)]. Letting the observer point be right at the output end of the crystal ( $z = L$ ), the incremental harmonic amplitude is

$$\begin{aligned} dA_2(x, y, L, t) &= \frac{-i\kappa A_0^2 \exp(i\Delta k z')}{\sqrt{(1-i\tau_x(L))(1-i\tau_y(L))(1-i\tau_x(z'))(1-i\tau_y(z'))}} \\ &\cdot \exp\left(-\frac{2(x-\rho L+\rho z')^2}{w_{0x}^2(1-i\tau_x(L))}\right) \exp\left(-\frac{2y^2}{w_{0y}^2(1-i\tau_y(L))}\right) \\ &\cdot \exp\left(-\frac{(4+i\alpha)\ln 2\left(t-\frac{L}{V_2}+\beta z'\right)^2}{t_p^2}\right) dz'. \end{aligned} \quad (10)$$

The harmonic field can be written as an integral over  $z'$  as given in (11), shown at the bottom of the page.

In principle, (11) can be used to calculate the output SH field profile. Because our intention is to derive a formula for the conversion efficiency, we do not actually need to calculate the field integral. First we write down the product of  $A_2$  and its complex conjugate. From (11), it can be written as a double integral. Then we can do some transformations using simple algebra to get the equations given in (12)–(15), shown at the bottom of the next page.

Defined by (15),  $l_{S-T}$  is what we call the generalized space-time walk-off length. In an SHG process with pulse sources, normally both temporal walk-off and spatial walk-off exist. Accordingly, people have defined the temporal walk-off length [14], the length over which the GVM would cause a time delay almost as long as the pulse duration, and the spatial walk-off length (called the aperture length in [7]), the length over which the spatial walk-off would cause a spatial shift almost as wide as the beam waist size. In our theory, the generalized walk-off length  $l_{S-T}$  represents a combination of both walk-off effects. It plays an important role in determining the conversion efficiency, as we will see in the equations later.

The pulse energy  $U_2$  of the harmonic wave can be acquired by an integral of field intensity over time and over the  $XY$  plane at  $z = L$

$$U_2 = \frac{1}{2}\varepsilon_0 c n_2 \int_{-\infty}^{\infty} dx \int_{-\infty}^{\infty} dy \int_{-\infty}^{\infty} dt |A_2(x, y, L, t)|^2. \quad (16)$$

Mathematically it can be proven that  $\int_{-\infty}^{\infty} \exp(-(x+C)^2/a^2) dx = \sqrt{\pi} |a|$  when  $a$  is real and  $C$  is any complex constant inside the integral. We can then substitute (12) into (16) and the integrals of  $x$ ,  $y$ , and  $t$  parts are all simple Gaussian integrals. The formula for  $U_2$  is

$$\begin{aligned} U_2 &= \varepsilon_0 c n_2 \frac{\pi^{3/2} \kappa^2 |A_0|^4}{16\sqrt{2}\ln 2} w_{0x} w_{0y} t_p \int_0^L \int_0^L \\ &\quad \exp(i\Delta k(z_1 - z_2)) \exp\left(-\frac{(z_1 - z_2)^2}{l_{S-T}^2}\right) dz_1 dz_2 \\ &\quad \cdot \frac{1}{\sqrt{(1-i\tau_x(z_1))(1-i\tau_y(z_1))(1+i\tau_x(z_2))(1+i\tau_y(z_2))}}. \end{aligned} \quad (17)$$

The fundamental pulse energy can be calculated from (8) as

$$U_1(0) = \varepsilon_0 c n_1 |A_0|^2 \frac{\pi^{3/2}}{8\sqrt{\ln 2}} w_{0x} w_{0y} t_p. \quad (18)$$

This is the energy of the input pulse, which remains constant throughout the SHG process as long as we assume no pump depletion.

From (17) and (18), we have the conversion efficiency in the case of no source depletion

$$\begin{aligned} \eta &= \frac{U_2}{U_1} \\ &= \sqrt{\frac{2\ln 2}{\pi}} \gamma \frac{U_1}{t_p} \frac{1}{\sqrt{b_x b_y}} \int_0^L \int_0^L \\ &\quad \exp(i\Delta k(z_1 - z_2)) \exp\left(-\frac{(z_1 - z_2)^2}{l_{S-T}^2}\right) dz_1 dz_2 \\ &\quad \cdot \frac{1}{\sqrt{(1-i\tau_x(z_1))(1-i\tau_y(z_1))(1+i\tau_x(z_2))(1+i\tau_y(z_2))}} \end{aligned} \quad (19)$$

where  $\gamma = 4\kappa^2 n_2 / \lambda_0 c \varepsilon_0 n_1 = 4\omega_1^2 d_{eff}^2 / n_1 n_2 \lambda_0 c^3 \varepsilon_0$ . We call this method to calculate the efficiency “the double-integral method.” Normally, the double integral can only be calculated numerically, but, in the special case of  $\Delta k = 0$  (phase-matching condition) and  $l_{S-T} \ll L \ll b_x$  &  $b_y$  (strong walk-off and weak focusing), it can be calculated analytically. In that case, the laser beam size is almost constant through the crystal, and

$$\begin{aligned} A_2(x, y, L, t) &= \frac{-i\kappa A_0^2}{\sqrt{(1-i\tau_x(L))(1-i\tau_y(L))}} \exp\left(-\frac{2y^2}{w_{0y}^2(1-i\tau_y(L))}\right) \\ &\quad \times \int_0^L \frac{\exp(i\Delta k z')}{\sqrt{(1-i\tau_x(z'))(1-i\tau_y(z'))}} \exp\left(-\frac{2(x-\rho L+\rho z')^2}{w_{0x}^2(1-i\tau_x(L))}\right) \exp\left(-\frac{(4+i\alpha)\ln 2\left(t-\frac{L}{V_2}+\beta z'\right)^2}{t_p^2}\right) dz' \end{aligned} \quad (11)$$

$\tau_x(z_1) = \tau_x(z_2) = \tau_x$ ,  $\tau_y(z_1) = \tau_y(z_2) = \tau_y$ . Thus,  $\tau_x$  and  $\tau_y$  only depend on the offset of the beam waist from the center of the crystal, but do not depend on  $z_1$  and  $z_2$ . Hence, they are constant for the integral. The double integral then only has a Gaussian term and it can be calculated when  $l_{S-T} \ll L$ . Since  $\Delta k = 0$  implies that  $n_1 = n_2 = n$ , the result is

$$\eta = \frac{U_2}{U_1} = \sqrt{2 \ln 2} \gamma \frac{U_1}{t_p} \frac{l_{S-T} L}{\sqrt{b_x b_y (1 + \tau_x^2)(1 + \tau_y^2)}}. \quad (20)$$

Note that in this case the harmonic pulse energy or efficiency is a linear function of crystal length. We can use this result to obtain a solution for arbitrary focusing (weak focusing not required) as long as the strong walk-off condition is maintained. When  $l_{S-T} \ll b_x$  and  $b_y$  and  $l_{S-T} \ll L$ , we can divide the crystal into small sections with length  $\Delta l$  ( $l_{S-T} \ll \Delta l \ll b_x$  and  $b_y$ ), use (20) for the harmonic energy generated in each section, and add them up to get the total output energy. The result can be written as a one-dimensional (1-D) integral

$$\eta_a = \frac{U_2}{U_1} = \sqrt{2 \ln 2} \frac{\gamma U_1}{t_p} l_{S-T} \int_0^L \frac{dz}{\sqrt{b_x b_y (1 + \tau_x^2(z))(1 + \tau_y^2(z))}}. \quad (21)$$

We can call this "the asymptotic method." When the fundamental beam is round, we have  $w_{0x} = w_{0y} = w_0$ ,  $b_x = b_y = b$ ,  $z_{0x} = z_{0y} = z_0$ , and  $\tau_x(z) = \tau_y(z) = \tau(z)$ . The integral can be calculated easily as

$$\eta_a = \frac{U_2}{U_1} = \sqrt{2 \ln 2} \frac{\gamma U_1 l_{S-T}}{2 t_p} \left[ \tan^{-1} \left( \frac{2(L - z_0)}{b} \right) - \tan^{-1} \left( \frac{-2z_0}{b} \right) \right]. \quad (22)$$

When the beam waist position is the same for  $X$  and  $Y$  directions and there is no source depletion, the best conversion efficiency should occur when the beam waist is at the center of the crystal ( $z_0 = L/2$ ). The result will be

$$\eta_{a \max} = \frac{U_2}{U_1} = \sqrt{2 \ln 2} \frac{\gamma U_1 l_{S-T}}{t_p} \tan^{-1} \left( \frac{L}{b} \right). \quad (23)$$

The subscript "a" means that this is given by the asymptotic method. Note that  $l_{S-T}$  and  $b$  both change with the beam waist size, unless there is no spatial walk-off (noncritical phase matching). In the special case of no spatial walk-off,  $l_{S-T}$  is only related to the temporal walk-off and (23) approaches a constant when the focusing is tight enough, which is consistent with the result in [14].

In the special case of no temporal walk-off (long pulse),  $l_{S-T} = w_{0x}/|\rho|$  is only related to the spatial walk-off. When the walk-off is large we can easily compare our results for round Gaussian beams with Boyd and Kleinman's CW results in [7]. There they defined the aperture length  $l_a = \sqrt{\pi} w_0/|\rho|$  and the effective length of focus  $l_f = \pi b/2$ . When  $l_{S-T} \ll L \ll b$  ( $l_a \ll L \ll l_f$ , large walk-off, weak focusing), the results are as follows:

$$\begin{aligned} \text{Ours from (20)} : \eta &= \sqrt{2 \ln 2} \frac{\gamma U_1}{t_p} \frac{l_{S-T} L}{b} \\ &= \sqrt{2 \ln 2} \frac{\gamma U_1}{t_p} \frac{w_0 L}{b |\rho|} \end{aligned} \quad (24a)$$

$$\begin{aligned} \text{Boyd and Kleinman's} : \eta &= \gamma \frac{P_\omega}{b} L l_a \\ &= \sqrt{\pi} \gamma P_\omega \frac{w_0 L}{b |\rho|} \end{aligned} \quad (24b)$$

where  $P_\omega$  is the CW power of the fundamental beam.

Likewise, when  $l_{S-T} \ll b \ll L$  ( $l_a \ll l_f \ll L$ , large walk-off, strong focusing), the results are as follows:

$$\begin{aligned} \text{Ours from (23)} : \eta &= \sqrt{2 \ln 2} \frac{\gamma U_1}{t_p} \frac{l_{S-T} \pi}{2} \\ &= \sqrt{2 \ln 2} \frac{\gamma U_1}{t_p} \frac{w_0 \pi}{2 |\rho|} \end{aligned} \quad (25a)$$

$$\begin{aligned} \text{Boyd and Kleinman's} : \eta &= \gamma \frac{P_\omega}{b} l_f l_a \\ &= \sqrt{\pi} \gamma P_\omega \frac{w_0 \pi}{2 |\rho|}. \end{aligned} \quad (25b)$$

We can clearly see that our results have the same form as those of Boyd and Kleinman, and the only difference comes

$$|A_2|^2 = \frac{\kappa^2 |A_0|^4}{\sqrt{(1 + \tau_x^2(L))(1 + \tau_y^2(L))}} \exp \left( -\frac{4y^2}{w_{0y}^2 (1 + \tau_y^2(L))} \right) \times \int_0^L \int_0^L \frac{\exp(i\Delta k(z_1 - z_2)) \exp \left( -\frac{4x_{12}^2}{w_{0x}^2 (1 + \tau_x^2(L))} \right) \exp \left( -\frac{8 \ln 2 t_{12}^2}{t_p^2} \right) \exp \left( -\frac{(z_1 - z_2)^2}{l_{S-T}^2} \right)}{\sqrt{(1 - i\tau_x(z_1))(1 - i\tau_y(z_1))(1 + i\tau_x(z_2))(1 + i\tau_y(z_2))}} dz_1 dz_2 \quad (12)$$

$$x_{12} = x - \rho L + \rho \frac{z_1 + z_2}{2} + \frac{i\tau_x(L)\rho(z_1 - z_2)}{2} \quad (13)$$

$$t_{12} = t - \frac{L}{V_2} + \beta \frac{z_1 + z_2}{2} - \frac{i\alpha\beta(z_1 - z_2)}{8} \quad (14)$$

$$l_{S-T} = \left( \frac{\rho^2}{w_{0x}^2} + \frac{(\alpha^2 + 16)\beta^2 \ln 2}{8t_p^2} \right)^{-1/2} \quad (15)$$

from how to define an effective power  $P_\omega$  for Gaussian pulses. The effective pulse duration can be defined by

$$\Delta t_{\text{eff}} = \frac{[\int dt I(t)]^2}{\int dt I^2(t)}. \quad (26)$$

The physical significance of  $\Delta t_{\text{eff}}$  is this: the generated SH energy by the Gaussian input pulse is the same as that which would be generated by a square input pulse with duration  $\Delta t_{\text{eff}}$  at peak power  $P_\omega = U_1/\Delta t_{\text{eff}}$ . For Gaussian pulses, we have from (8) that  $\Delta t_{\text{eff}} = (\pi/2 \ln 2)^{1/2} t_p$ . With these results, (24a) and (25a) from our formulation become exactly the same as (24b) and (25b), which are from [7].

We have introduced our theory under the nondepleted assumption. In the next section, we will extend it into the depletion region.

### III. CONVERSION EFFICIENCY WITH SOURCE DEPLETION

We have derived the formula for the type-I SHG efficiency under the no-source-depletion approximation. We already have a relationship between the harmonic pulse energy, fundamental pulse energy, and the crystal length in that region, which we can write in the following form:

$$U_2 = U_1^2 F(L). \quad (27)$$

$F(L)$  is a function of crystal length  $L$ . The function is also related to the laser field profile and material properties. In our theory it is just the right-hand side of (19) without  $U_1$ . From (27), we can derive a differential relationship

$$\frac{dU_2}{dz} = U_1^2 F'(z) \quad (28)$$

where  $F'(z)$  is derivative of  $F(z)$  with respect to  $z$ . It shows that the increasing rate of the harmonic energy over a small segment of crystal is proportional to the square of fundamental pulse energy and  $F'(z)$ . Physically  $F'(z)$  should be determined by the field boundary conditions (field spatial and temporal profile on the boundaries) of each  $dz$  slab we are studying. Equation (28) was derived from the no-pump-depletion case. However, we can approximately treat pump depletion if we assume that (28) remains unchanged with the same  $F'(z)$  as in the no-source-depletion approximation. This is equivalent to ignoring the change of boundary conditions for the  $dz$  slab, which includes the nonlinear reshaping of the fundamental spatial and temporal field profile and the co-existence of the harmonic field with the fundamental field at the slab boundary. The strong walk-off in our experiments can separate the fundamental field and the generated harmonic field, which may improve the validity of this approximation relative to the weak walk-off case. One might expect this approximation to fail under very heavy pump depletion, since the nonlinear process will deplete the stronger part of the fundamental field more than the weaker part and reshape the field profile. We will discuss how well this approximation works with increasing pump depletion in Section V.

With this approximation, we use the following coupled equations:

$$\frac{dU_2}{dz} = U_1^2 F'(z) \quad (29a)$$

$$\frac{dU_1}{dz} = -\frac{dU_2}{dz} \quad (29b)$$

where (29b) comes from energy conservation. We can substitute (29b) into (29a) and obtain a single differential equation of  $U_1(z)$ .  $U_1(L)$  can be easily solved and  $U_2(L) = U_1(0) - U_1(L)$ . The result is

$$\eta = \frac{U_2(L)}{U_1(0)} = 1 - \frac{1}{1 + U_1(0)F(L)} = 1 - \frac{1}{1 + \eta_{md}}$$

or

$$\frac{1}{1 - \eta} = 1 + \eta_{md}. \quad (30)$$

$\eta$  now is the efficiency including source depletion,  $U_1(0)$  is the input fundamental pulse energy,  $U_1(0)F(L)$  is the efficiency we get if assuming no source depletion, and we can call it  $\eta_{md}$ .  $\eta_{md}$  corresponds to the equations we derived in the previous section. Normally, when we work in the depletion region, if we try to calculate the efficiency assuming no source depletion, we will get a result ( $\eta_{md}$ ) over 100%, which is physically meaningless. Equation (30) always gives a conversion efficiency between 0 and 1. When  $\eta$  or  $\eta_{md} \ll 1$ , we will have  $\eta = \eta_{md}$ , which means that SHG is in the nondepletion region and our results in the previous section can be used directly. Note that, in (30),  $\eta$  increases monotonically with  $\eta_{md}$ . This means that in this theory the optimal SHG condition (focusing and phase mismatch, etc.) is the same whether source depletion is considered or not. For example, if the beam waist position is the same for  $X$  and  $Y$  directions (always true for round beams), the optimal beam waist position remains at the crystal center even with pump depletion. This will be further discussed in Sections V and VI.

Under this same approximation, we can now easily transform formulas derived in the nondepletion region for use in the depletion region. The double-integral method for type-I SHG efficiency will be

$$\frac{1}{1 - \eta} = 1 + \sqrt{\frac{2 \ln 2}{\pi}} \gamma \frac{U_1(0)}{t_p} \frac{1}{\sqrt{b_x b_y}} \cdot \iint_{0 \rightarrow L} \frac{\exp(i\Delta k(z_1 - z_2)) \exp\left(-\frac{(z_1 - z_2)^2}{l_{S-T}^2}\right) dz_1 dz_2}{\sqrt{(1 - i\tau_x(z_1))(1 - i\tau_y(z_1))(1 + i\tau_x(z_2))(1 + i\tau_y(z_2))}}. \quad (31)$$

The result of the asymptotic method is

$$\frac{1}{1 - \eta_a} = 1 + \sqrt{2 \ln 2} \gamma \frac{U_1(0)}{t_p} l_{S-T} \cdot \int_0^L \frac{dz}{\sqrt{b_x b_y (1 + \tau_x^2(z))(1 + \tau_y^2(z))}}. \quad (32)$$

With a round Gaussian beam it is

$$\frac{1}{1 - \eta_a} = 1 + \sqrt{2 \ln 2} \gamma \frac{U_1(0)}{t_p} l_{S-T} \cdot \frac{1}{2} \left[ \tan^{-1} \left( \frac{2(L - z_0)}{b} \right) - \tan^{-1} \left( -\frac{2z_0}{b} \right) \right]. \quad (33)$$

Furthermore, if the beam waist of the round beam is at the crystal center, then we have

$$\frac{1}{1 - \eta_{a \max}} = 1 + \sqrt{2 \ln 2} \gamma \frac{U_1(0)}{t_p} l_{S-T} \tan^{-1} \left( \frac{L}{b} \right). \quad (34)$$

Equations (31) and (32) are used in our theoretical calculation of SHG efficiency.

## IV. NUMERICAL CALCULATIONS

To put the theory to the test, we need to calculate the efficiency using the above equations. In our experiments, the input laser beam has an elliptical cross section, so (31) and (32) were used. Before doing the numerical calculation we define a few dimensionless parameters:  $q = w_{0x}/w_{0y} = (b_x/b_y)^{1/2}$  represents the ellipticity;  $\sigma = L/l_{S-T}$  is a measure of the crystal length relative to the generalized walk-off length;  $\mu = L/b_x$  is a comparison between the crystal length and the confocal parameter;  $\Delta\phi = \Delta kL$  is the total phase mismatch over the crystal;  $f_0 = 2(L/2 - z_{0x})/b_x$  is the distance between crystal center and  $x$  beam waist position normalized to  $x$  depth of focus;  $f_d = 2(z_{0x} - z_{0y})/b_x$  is the distance between the beam waist positions in  $x$  and  $y$  directions normalized to  $x$  depth of focus (positive means that the  $x$  beam waist is closer to the output end). Simple algebra shows that  $\tau_y(z) = q^2(\tau_x(z) + f_d)$  for any  $z$ . Let  $\tau_x(z_1) = \tau_{x1}$  and  $\tau_x(z_2) = \tau_{x2}$  in (31), and (31) can be transformed into (35), shown at the bottom of the page.

Let  $\tau_x(z) = \tau_x$  in (32), and (32) can be transformed into

$$\frac{1}{1 - \eta_a} = 1 + \sqrt{2 \ln 2} \frac{\gamma U_1(0)}{t_p} l_{S-T} \frac{q}{2} \int_{f_0 - \mu}^{f_0 + \mu} \frac{d\tau_x}{\sqrt{(1 + \tau_x^2)(1 + q^4(\tau_x + f_d)^2)}}. \quad (36)$$

Again the subscript "a" means the asymptotic method. The integrals in the above equations use all dimensionless parameters. If we assume that the beam waist is at the crystal center, the integral would be from  $-\mu$  to  $+\mu$ .

We studied the dependence of conversion efficiency on total phase mismatch  $\Delta\phi$  using (35) assuming a round beam ( $q = 1$ ,  $f_d = 0$ ). The work in [7] showed that in the CW case the optimal efficiency may occur at nonzero phase-mismatch due to vector phase matching, while the efficiency versus  $\Delta\phi$  behavior changes dramatically with different  $L/b$  values. In our pulsed case, the  $\eta$  versus  $\Delta\phi$  curve depends on two parameters:  $L/l_{S-T}$  and  $L/b$ , which we defined as  $\sigma$  and  $\mu$  above. Using (35), assuming  $z_0 = L/2$  (or  $f_0 = 0$ , optimal beam waist position),  $L = 8$  mm,  $d_{\text{eff}} = 2$  pm/V,  $t_p = 100$  fs and  $U_1 = 3.75$  nJ, we calculated efficiency versus  $\Delta\phi$  curves for different  $L/l_{S-T}$  and  $L/b$  values. The results are shown in Fig. 2. We found that there are basically three regions. In Region 1 we have  $L/l_{S-T} < 1$  and  $L/b < 1$  (weak walk-off and weak focusing). The efficiency versus  $\Delta\phi$  curve has an oscillating feature similar to a sinc<sup>2</sup> function and is basically symmetrical (but with the central peak occurring for some  $\Delta\phi < 0$ ). An example is shown in Fig. 2(a). Region 2 is characterized by  $L/b \gg 1$  and  $L/b > L/l_{S-T}$  (strong focusing and the walk-off length is longer than the confocal parameter). In this region, the curves still have an oscillating feature but it is far from symmetrical, as shown in Fig. 2(b). In Region 3 we have  $L/l_{S-T} \gg 1$  and  $L/l_{S-T} > L/b$  (strong walk-off and the confocal parameter is longer than the walk-off length). In this region, the curves

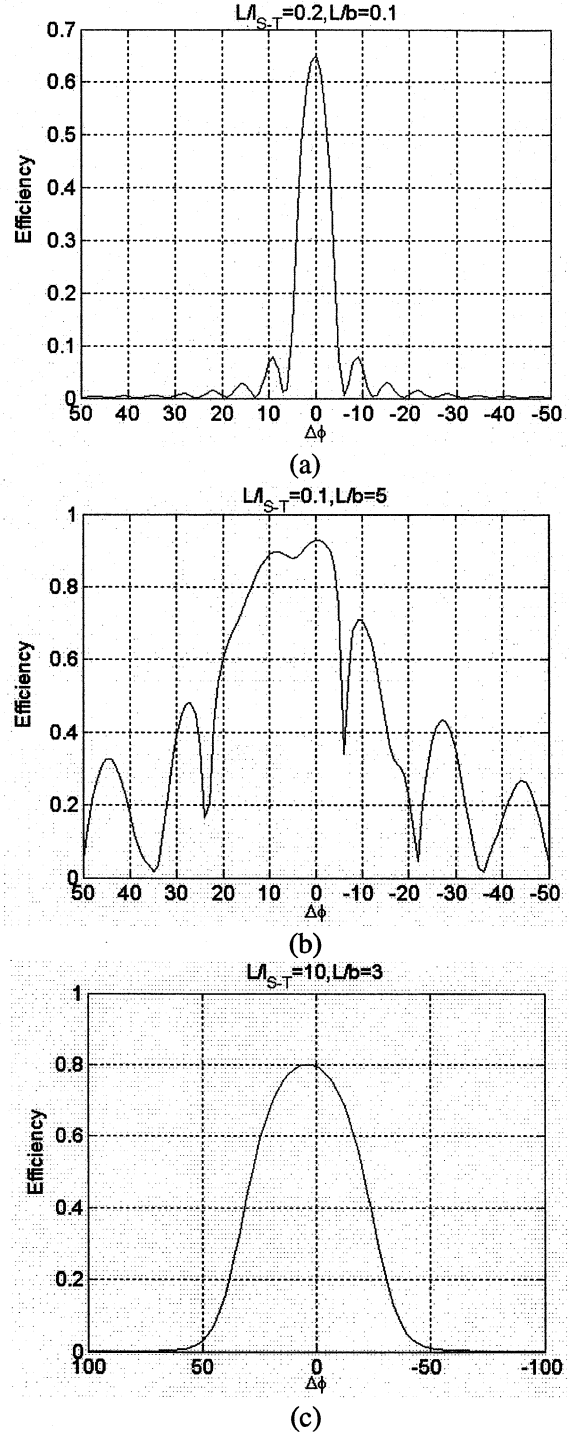


Fig. 2. The efficiency versus  $\Delta\phi$  ( $= \Delta kL$ ) behavior based on (35). We used the nonlinear coefficient of the BBO crystal. A round input beam and 300-mW input power was assumed.

look like a single wide peak with no oscillation, as in Fig. 2(c). In this region, the optimal efficiency still takes place for  $\Delta k < 0$ , however, the efficiency at  $\Delta k = 0$  is very close to the optimal

$$\frac{1}{1 - \eta} = 1 + \sqrt{\frac{2 \ln 2}{\pi}} \frac{\gamma U_1(0)}{t_p} \frac{qL}{4\mu} \int_{f_0 - \mu}^{f_0 + \mu} \int_{f_0 - \mu}^{f_0 + \mu} \frac{e^{i\Delta\phi(\tau_{x1} - \tau_{x2})/2\mu} e^{-\sigma^2(\tau_{x1} - \tau_{x2})^2/4\mu^2} d\tau_{x1} d\tau_{x2}}{\sqrt{(1 - i\tau_{x1})(1 - iq^2(\tau_{x1} + f_d))(1 + i\tau_{x2})(1 + iq^2(\tau_{x2} + f_d))}}. \quad (35)$$

efficiency. We also did calculations using the ellipticity from our experiments ( $q = 0.6$ ), which showed a similar  $\eta$  versus  $\Delta\phi$  behavior. Since our experiments turn out to be all in Region 3, we assumed  $\Delta\phi = 0$  in predicting the optimal efficiencies for our experiments. The error arising from this approximation should be very small.

We also studied the focusing dependence of SHG efficiency using (36) assuming round beam ( $q = 1$ ,  $f_d = 0$ ), phase matching ( $\Delta k = 0$ ), and optimal beam waist position ( $f_0 = 0$ ). Basically we wish to calculate  $\eta$  versus  $\mu$  curves. Based on (35), it is clear that how  $\sigma$  and  $\mu$  are related (or, equivalently, how  $l_{S-T}$  and  $b$  are related) is a key factor that determines the shape of the curve. From (15), we have

$$\sigma = \sqrt{A^2 + 4B^2\mu} \quad (37a)$$

$$A = \sqrt{\frac{(\alpha^2 + 16) \ln 2 \beta L}{8}} \frac{\beta L}{t_p} \quad (37b)$$

$$B = \frac{\rho \sqrt{k_1 L}}{2}. \quad (37c)$$

The parameter “ $A$ ” represents the effect of temporal walk-off and “ $B$ ” represents spatial walk-off. In the CW case, the work in [7] also used a “ $B$ ” parameter in the studying of focusing dependence, which is the same as our “ $B$ ,” The “ $A$ ” and “ $B$ ” parameters come naturally from the definition of the generalized walk-off length.

Based on (35), we now define a dimensionless function  $h_m(A, B, \mu)$  as

$$h_m(A, B, \mu) = \frac{1}{4\mu} \int_{-\mu}^{\mu} \int_{-\mu}^{\mu} \frac{e^{-\sigma^2(\tau_{x1} - \tau_{x2})^2/4\mu^2} d\tau_{x1} d\tau_{x2}}{(1 - i\tau_{x1})(1 + i\tau_{x2})}. \quad (38)$$

This function can be viewed as an extension of  $h_m(B, L/b)$  in [7]. It determines the focusing dependence of the SHG efficiency assuming a round input Gaussian beam, perfect phase matching, and that the input beam waist is at the crystal center (optimal position in theory). Some  $h_m(A, B, L/b)$  versus  $L/b$  curves are shown in Fig. 3 for several different  $A$  and  $B$  values. Some features are: larger  $A$  (larger temporal walk-off) decreases efficiency and causes the optimal  $L/b$  to be larger (tighter focusing); larger  $B$  (larger spatial walk-off) decreases efficiency and causes the optimal  $L/b$  to be smaller (looser focusing). In the limit of  $B \gg A$  and  $B \gg 1$ , it seems that the optimal  $L/b$  approaches a value of  $\sim 1.4$ . This is consistent with the result in [7], which shows that, in the limit of large  $B$ , the optimal  $L/b$  is approximately 1.39. It is worth mentioning that, in the case of noncritical phase matching ( $B = 0$ ), the asymptotic method [(34)] and our previous study [14] suggested that the efficiency will approach a high limit with very tight focusing. However, this is not true based on our full theory (double-integral method: (19), (31), and (35)), as we can see from Fig. 3. Even if  $B = 0$  (no spatial walk-off), the efficiency still has a peak and goes down with tighter focusing. This is because the asymptotic method and the theory in [14] were derived under the assumption  $l_{S-T} < b$ , which is inevitably violated with  $B = 0$  and very strong focusing. However, the asymptotic method still works almost just as well as the full theory in most cases, as we will see in the next section. In our experiments, for the BBO

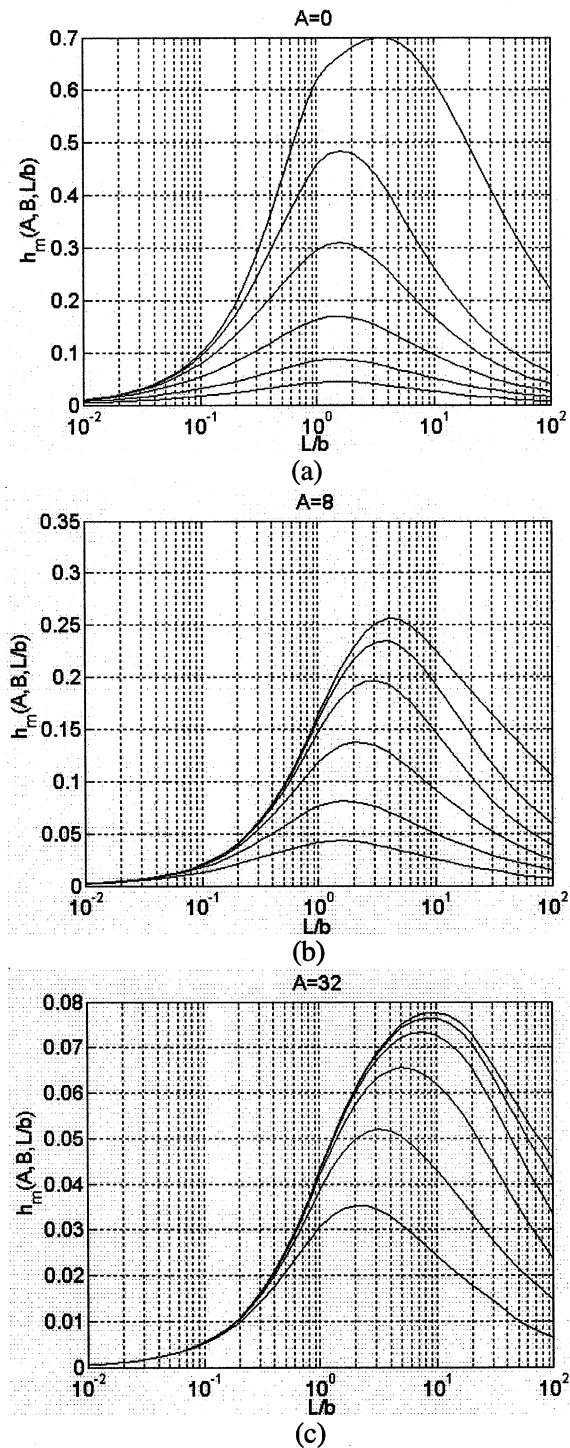


Fig. 3.  $h_m(A, B, L/b)$  versus  $L/b$  curves for different  $A$  and  $B$  values.  $A = 0, 8$ , and  $32$ , as indicated in the figures. In each figure, the six curves corresponds to  $B = 0, 1, 2, 4, 8$ , and  $16$ , from the highest to the lowest, respectively.

crystal we have  $A = 13$ ,  $B = 10.5$ , and  $L/b$  goes from  $0.6$  to  $25$ ; for LBO we have  $A = 15$ ,  $B = 3$ , and  $L/b$  goes from  $1.2$  to  $50$ .

To predict the optimal efficiencies for modeling our experiments, we assumed  $\Delta k = 0$  as we stated above. However, for elliptical beams, the optimal beam waist position (or optimal  $f_0$ ) depends on  $f_d$  (the distance between  $x$  and  $y$  beam waist positions). In our theory, the optimal  $f_0$  should be between  $0$  and

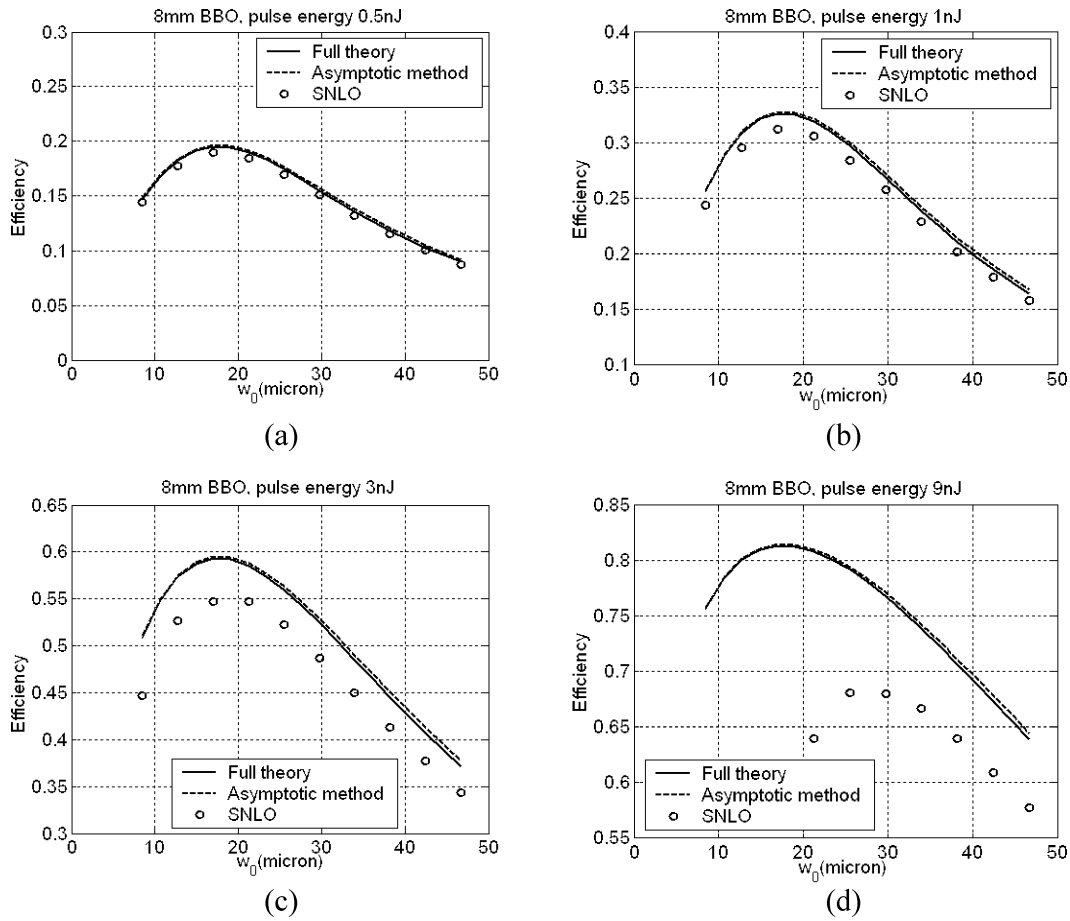


Fig. 4. Comparison between our theoretical results and numerical model SNLO with the same inputs and the properties of 8-mm BBO crystal. (a) Input pulse energy 0.5 nJ, (b) 1 nJ, (c) 3 nJ, and (d) 9 nJ. Note that the vertical scale in some figures does not start from 0, so the relative difference will be smaller than it seems to be.

$-f_d$ , which means that the crystal center is somewhere between the two beam waist positions. We do not have an analytical relationship between optimal  $f_0$  and  $f_d$ , but we did numerically estimate it for our experiments and included this relationship in our program, as we will describe later. We use Matlab6 to evaluate (35) or (36) and compare the results with experimental data.

## V. COMPARISON BETWEEN THEORETICAL AND NUMERICAL MODELS

As we mentioned in the introduction section, a software code named SNLO developed by Sandia National Laboratories [15], [16] includes a numerical model which can deal with short pulse mixing of round Gaussian beams. We compared the results of our theory [(35) and (36)] with those of the numerical model with the same inputs for a type-I SHG process. The inputs we used are: fundamental wavelength of 800 nm; harmonic wavelength of 400 nm; FWHM input pulse duration of 100 fs; refractive index of 1.66, fundamental group velocity index of 1.6845, harmonic group velocity index of 1.7426 (corresponding to 193 fs/mm GVM); fundamental walk-off angle of 0, harmonic walk-off angle of 67.7 mrad;  $d_{\text{eff}} = 2$  pm/V; crystal length of 8 mm;  $\Delta k = 0$ . Spreading of the input fundamental pulse due to group velocity dispersion, loss and surface reflections, and other nonlinear factors such

as the Kerr effect and two-photon absorption are all set to zero. The material properties are in fact from our BBO crystal (calculated from the nonlinear coefficients from [18] and Sellmeier equations from [19]). The SNLO code has been carefully benchmarked in the literature in OPO studies under loose focusing conditions [15]. Although we were unable to find studies in the literature testing SNLO under focusing as tight as in our experiments, with a proper grid and step size it should provide useful results with which to compare our theory.

Assuming that the beam waist of the round Gaussian beam is at the crystal center, we calculated the conversion efficiency for different beam waist sizes and different input pulse energy. The results are shown in Fig. 4 (the  $X$  axis in the figures are the  $e^{-2}$  intensity beam waist radius). As we can see, when the input pulse energy is low (0.5 nJ and 1 nJ figures), the SHG is in the low pump depletion region, and SNLO results fit our theory perfectly. This is an evidence that our theory is accurate in the nondepletion region. In Fig. 4(b), the best efficiency is actually over 30%.

In Fig. 4(c) and (d), the SHG is in the depletion region. We can see that our theory overestimated the efficiency comparing with SNLO in that region. It is because in our treatment of the pump depletion, we ignored the nonlinear reshaping of the fundamental field. The nonlinear reshaping flattens the fundamental field, and the flattened field yields smaller efficiency

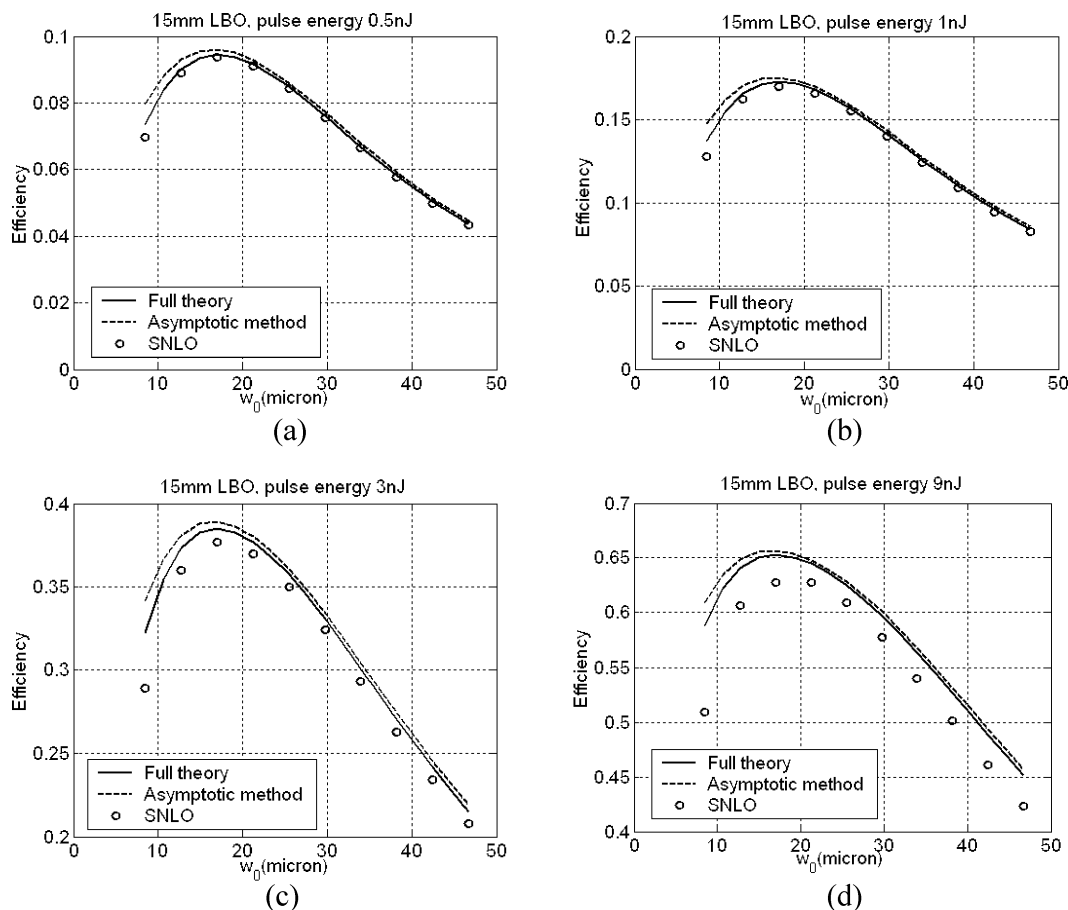


Fig. 5. The comparison between our theoretical results and numerical model SNLO with the same inputs and the properties of 15-mm LBO crystal. (a) input pulse energy 0.5 nJ, (b) 1 nJ, (c) 3 nJ, and (d) 9 nJ.

comparing with Gaussian field with the same total energy. So ignoring the nonlinear reshaping will obviously result in overestimating the efficiency. As a result, in Fig. 4(c), we see that the shape of the curves still fit quite well, but our theoretical results are generally a few percent higher than SNLOs results. In Fig. 4(c), the efficiencies are already close or higher than 50%. In Fig. 4(d), the differences become much larger because higher pulse energy makes the nonlinear reshaping of the pump field happen much faster, and so ignoring it is no longer acceptable for most part of the SHG process.

We also did a comparison with the parameters of our LBO crystal. The inputs are: refractive index 1.60, fundamental group velocity index 1.6315, harmonic group velocity index 1.6686 (corresponding GVM 124 fs/mm); fundamental walk-off angle 0, harmonic walk-off angle 16.6 mrad;  $d_{\text{eff}} = 0.723$  pm/V; crystal length 15 mm. The LBO properties are calculated from the nonlinear coefficients from [18] and Sellmeier equations from [20]. All other inputs are the same as the previous calculation. The results are in Fig. 5, which basically reveals the same phenomena as in Fig. 4, but for the LBO the curves still fit quite well even for 9-nJ pulse energy (the efficiency is as high as 60%). This is because LBO has a much smaller nonlinearity than BBO, and so the nonlinear reshaping of the pump field happens much more slowly for the same pulse energy.

Since our theory is an extension of Boyd and Kleinman's theory [7], we decided to compare the calculated efficiency of a CW Gaussian input using Boyd and Kleinman's theory and SNLO. The results are shown in Fig. 6 for both crystals. Basically, they fit perfectly as well. This is strong evidence that both models are accurate in the nondepletion region.

We further use SNLO to calculate the optimal beam waist position for different pulse energies. We know that, for a round input beam and without pump depletion, the optimal beam waist is at the crystal center, which is a fact in both our theory and Boyd&Kleinman's theory. As we mentioned, in our theory the optimal beam waist position is always at the crystal center for a round input beam regardless of the depletion, which is a result of ignoring the nonlinear reshaping caused by depletion. Here we use SNLO to study how the optimal beam waist changes with the input pulse energy if the nonlinear reshaping is taken into account. We still assume that the input is a round Gaussian beam, and the beam waist diameter is  $35 \mu\text{m}$  (the corresponding  $e^{-2}$  beam radius is  $29.7 \mu\text{m}$ ) in an 8-mm BBO crystal. The results are shown in Fig. 7. In Fig. 7, for 1- and 3-nJ input pulse energies, the optimal beam waist positions appear to be at the crystal center, or at least very close to it. For 3-nJ pulse energy, the efficiency is already near 50%. For higher input pulse energies, the optimal beam waist position moves to the input end of

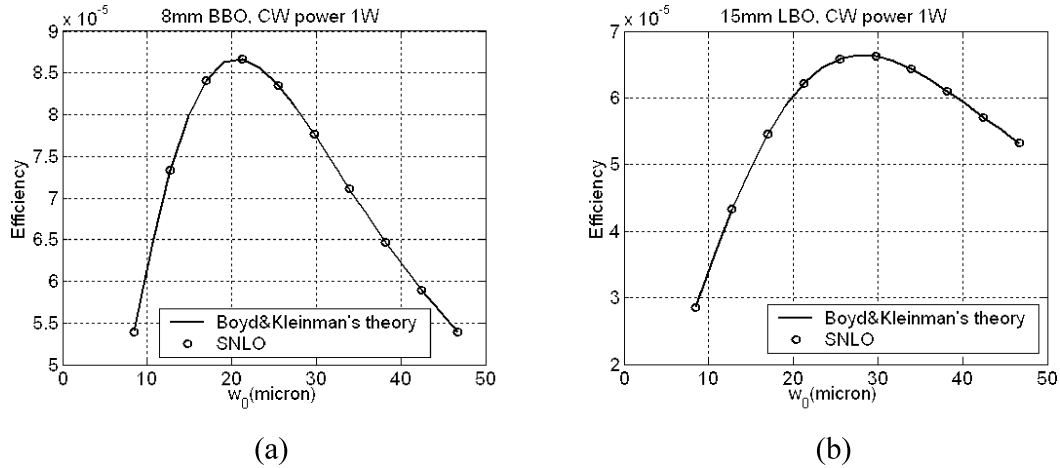


Fig. 6. The comparison between Boyd and Kleinman's theory and SNLO with the same inputs and the properties from both crystals: (a) 8-mm BBO and (b) 15-mm LBO.

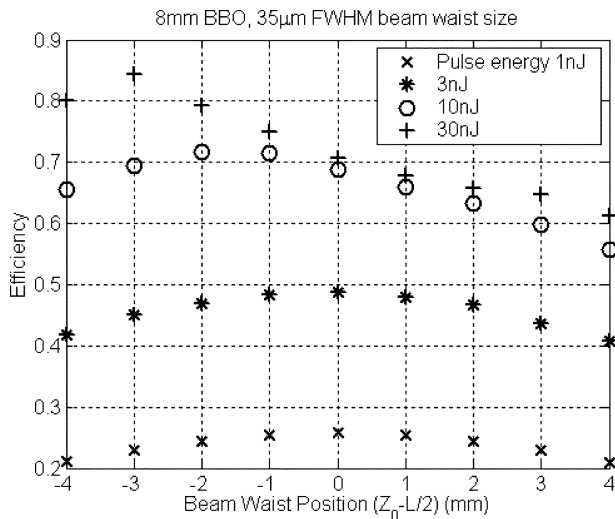


Fig. 7. Efficiency versus beam waist position for 8-mm BBO, 35- $\mu\text{m}$  FWHM beam waist diameter and various input pulse energies. The beam waist is at the input end of crystal if  $(z_0 - L/2) = -4$  mm, the center if  $(z_0 - L/2) = 0$ , and the output end of crystal if  $(z_0 - L/2) = 4$  mm.

the crystal. For 10 nJ, it is somewhere between  $-1$  and  $-2$  mm; for 30 nJ it is near  $-3$  mm (only 1 mm away from the input end). This is understandable because, to achieve better efficiency, the high peak intensity at the beam waist is better to be utilized before the nonlinear reshaping happens (which flattens the field profile and reduces the peak intensity). So the optimal beam waist should be expected to move to the input side for higher input pulse energy.

Based on the above comparisons, we have seen that our theory and SNLO agree extremely well in the nondepletion region. In the depletion region, they still agree quite well with efficiencies up to 50%. Further pump depletion will enlarge the discrepancies because our treatment in the depletion region ignores the nonlinear reshaping of the pump field. In Section VI, we will compare our theoretical results and experimental data for the 8-mm BBO and 15-mm LBO. Since we used elliptical beams in our experiments, it is not possible to use SNLO to simulate the experimental results.

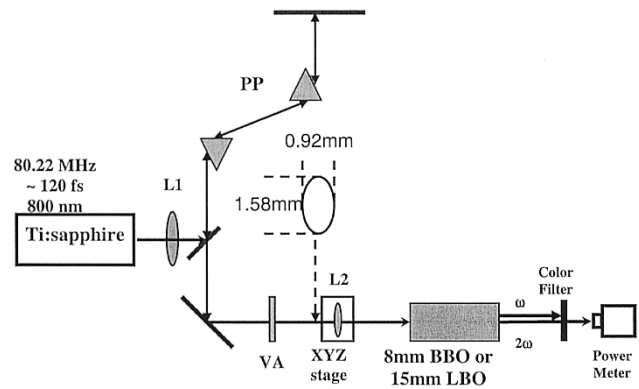


Fig. 8. The experimental setup. PP: prism pair. VA: variable attenuator. L1, L2: lenses.

## VI. EXPERIMENTAL RESULTS AND DISCUSSION

We have also performed experimental measurements with long crystals for comparison. The experimental setup is shown in Fig. 8. The input is from a mode-locked Ti:sapphire Laser (Spectra Physics Tsunami) with a center wavelength of 800 nm (near IR) and a repetition rate of 80 MHz. The lens L1 is a long-focal-length lens that we use to control the beam size. The prism pair is for dispersion compensation. The optimized pulse has a duration ( $t_p$  in the theory) of 122 fs FWHM, estimated from autocorrelation measurements. The variable attenuator is to control the input power to the nonlinear crystal. The best input power we could get was a little over 900 mW. The lens L2 is the input lens which focuses the fundamental beam into the crystal. We measured the beam profile at different locations and its propagation matches that of an elliptical Gaussian beam. Right before the input lens, the FWHM beam width in intensity is 0.919 mm in the horizontal ( $y$ ) direction and 1.58 mm in the vertical ( $x$ ) direction; the horizontal beam waist is 1.022 m before the lens and the vertical beam waist is 1.086 m before the lens. Knowing the focal length of the input lens and the beam profile, we then can calculate the  $e^{-2}$  intensity beam waist radius, beam waist position, and depth of focus in both the  $x$  and

TABLE I  
CALCULATED GAUSSIAN BEAM PARAMETERS AFTER FOCUSING FOR DIFFERENT LENSES IN OUR EXPERIMENTS.  
THE PARAMETERS ARE DEFINED IN (8) AND THE TEXT

F(mm)	$w_{0x}(\mu\text{m})$	$w_{0y}(\mu\text{m})$	$b_x(\text{mm})$	$b_y(\text{mm})$	$(z_{0x}-z_{0y})/b_x$	$(z_{0x}-z_{0y})/b_y$
25	4.91	8.34	0.189	0.546	1.0975	0.3799
31	6.12	10.38	0.294	0.846	1.0987	0.3818
36	7.14	12.10	0.400	1.150	1.0996	0.3835
50	10.06	16.95	0.795	2.256	1.1021	0.3881
65	13.28	22.26	1.385	3.892	1.1047	0.3931
80	16.60	27.66	2.164	6.009	1.1071	0.3984
100	21.18	35.04	3.523	9.643	1.1100	0.4056
140	30.96	50.39	7.528	19.94	1.1148	0.4209

$y$  directions after focusing by considering the transformation of the Gaussian beam through the lens. The lenses we used in the experiments have eight different focal lengths: 25, 31, 36, 50, 65, 80, 100, and 140 mm. The calculated results are listed in Table I. The parameters in Table I were defined in (8) and the following paragraph. After entering the crystal, the Gaussian beam waist size remains unchanged, but the position of the waist will be shifted by an amount proportional to the refractive index. So, in the crystals,  $b_x$  and  $b_y$  values in Table I should be multiplied by the refractive index of the crystal, but all the other values remain the same. The nonlinear crystal is either an 8-mm BBO crystal or 15-mm LBO crystal (provided by U-Oplaz, formerly known as CASIX). They are cut for type-I SHG at 800 nm. For BBO,  $\theta = 29.18^\circ$ ,  $\phi = 90^\circ$  (in the conventional coordinate system as in [18]),  $n = 1.66$ ,  $\rho = 3.9^\circ$ ,  $d_{\text{eff}} = 2 \text{ pm/V}$  [18],  $\beta = 193 \text{ fs/mm}$ ; For LBO,  $\theta = 90^\circ$ ,  $\phi = 31.7^\circ$ ,  $n = 1.61$ ,  $\rho = 0.95^\circ$ ,  $d_{\text{eff}} = 0.723 \text{ pm/V}$  [18],  $\beta = 124 \text{ fs/mm}$ . The walk-off angle, refractive index, and GVM are calculated from the Sellmeier equations [19], [20]. The generated SH light has a wavelength centered near 400 nm (blue). Both crystals are AR-coated at 400 and 800 nm on both ends. The blue output power was detected after a color filter. Within the accuracy of our measurements, we did not observe any linear or nonlinear absorption in the crystals.

We need to calculate the optimal efficiency we can get from the crystals under certain input power and certain focusing using our theory. As we mentioned in Section IV, we set  $\Delta k = 0$  in calculation. However, to calculate the optimal efficiency we must know the optimal beam waist position. For a round beam we know that it is the crystal center in our theory ( $f_0 = 0$ ), but for elliptical beams the theoretical optimal beam waist position (optimal  $f_0$ ) depends on the focusing and the distance between the  $x$  and  $y$  beam waists ( $f_d$ ) [see (35)]. From Table I we can see that  $(z_{0x} - z_{0y})/b_x = f_d/2$  is almost constant at 1.1, so  $f_d$  can be considered as a constant at 2.2 in our cases. Setting  $f_d = 2.2$  in (35), we numerically calculated the efficiency versus  $f_0$  curve for each lens we used, and from these curves we get the optimal  $f_0$  for each lens. Then we construct an approximate function describing the dependence of the optimal  $f_0$  on the lens focal length, so that we can calculate the approximate optimal value of  $f_0$  for any lens with the focal length  $F$  between 25 and 140 mm. We included this dependence in our program, and in this way we can calculate a continuous curve of optimal efficiency versus  $F$  (or the beam radius  $w_{0x}$  in crystal, equivalently). The approximate optimal  $f_0$  versus  $F$  functions are: for BBO, if  $F < 80 \text{ mm}$ ,  $f_0/f_d = -0.3$ ;  $f_0/f_d$  goes from

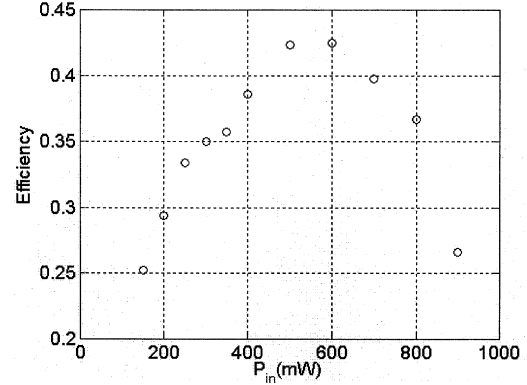


Fig. 9. The efficiency versus input power data points, BBO crystal, when other experimental conditions except input power are fixed to give maximum efficiency at 250-mW input power.

$-0.3$  to  $-0.2$  linearly with respect to  $F$  as  $F$  goes from 80 to 100 mm;  $f_0/f_d$  goes from  $-0.2$  to  $-0.1$  linearly with respect to  $F$  as  $F$  goes from 100 to 140 mm. For LBO, if  $F < 80 \text{ mm}$ ,  $f_0/f_d = -0.4$ ;  $f_0/f_d$  goes from  $-0.4$  to  $-0.3$  linearly with respect to  $F$  as  $F$  goes from 80 to 100 mm;  $f_0/f_d$  goes from  $-0.3$  to  $-0.2$  linearly with respect to  $F$  as  $F$  goes from 100 to 140 mm. With the above approximate optimal  $f_0$  versus  $F$  curves, the calculated optimal efficiencies are within 0.1% to the real optimum in our theory, which we think is good enough. Note that the crystal center is always somewhere between the optimal  $X$  and  $Y$  beam waist positions in our theory. In our experiments it means that the optimal  $X$  beam waist position is between the crystal center and the output end at low input powers (the nondepletion region).

We studied the SHG efficiencies under different input lenses and input powers. First we did an experiment with the 140-mm focal-length lens and the BBO crystal. We optimized the SHG efficiency under a relatively low input power (250 mW) by tuning the prism pair, the position of the input lens and the orientation of the crystal. The measurements showed that at the optimized crystal position, the focused beam waist is approximately at the crystal center. We then fixed the position of the input lens and crystal and increased the input power. We found that the conversion efficiency first increased, reached a maximum of  $\sim 43\%$  at around 600 mW input power, and then dropped under higher input powers. No power loss was observed in the experiments even when the input power is 900 mW (the total output power of the IR and blue pulses are within 2% difference from the input power, which is within the

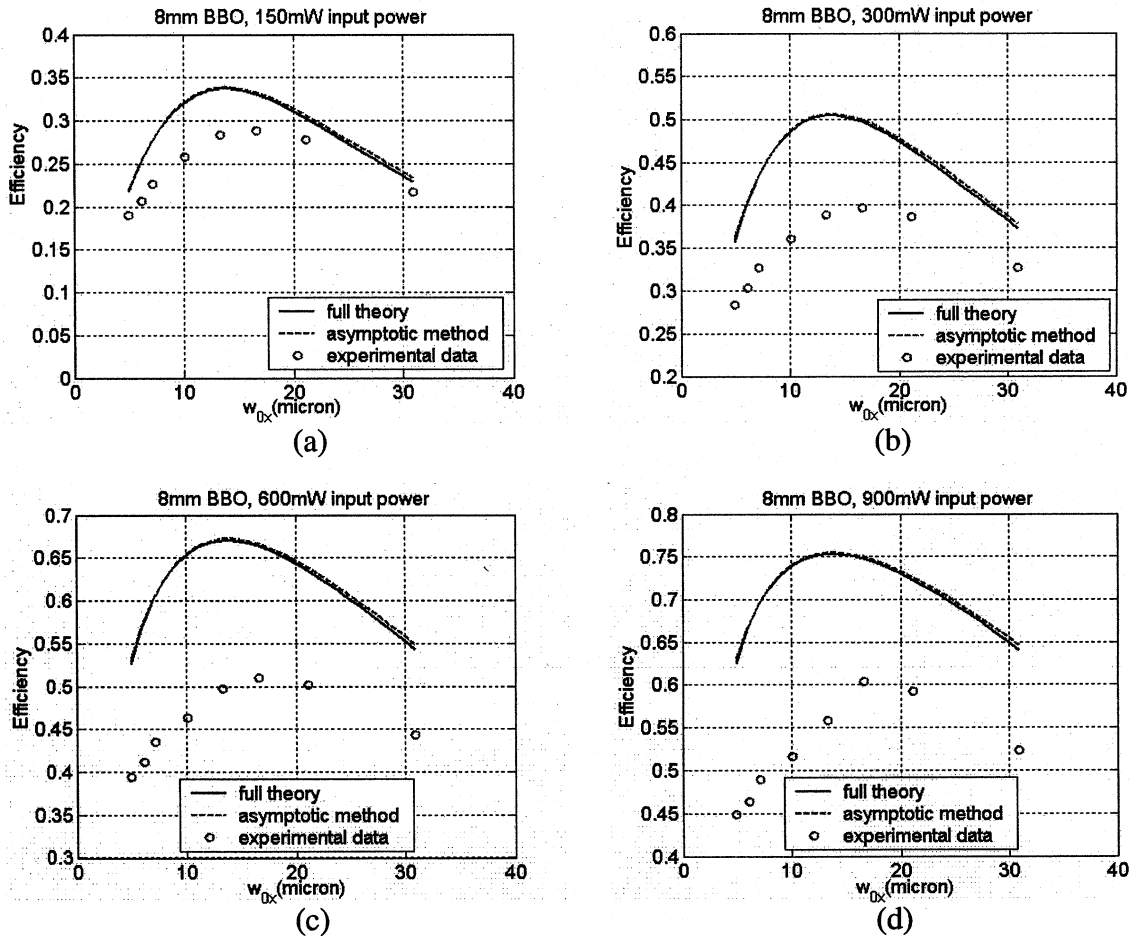


Fig. 10. The focusing dependence of optimal efficiency for BBO under different input powers: (a) 150 mW (or 1.875 nJ pulse energy), (b) 300 mW (3.75 nJ), (c) 600 mW (7.5 nJ), and (d) 900 mW (11.25 nJ).  $w_0$  is the  $e^{-2}$  intensity beam waist radius. The solid curves are the results of the double-integral method; the dashed curves are the results of the simplified method; the circles are the data points.

measurement error range). Fig. 9 shows the efficiency versus input power data for this measurement.

We also found that the drop in efficiency at high input power is related to the change of the optimal beam waist position (or optimal input lens position in experiments) with input power. If we optimized the output power at a relatively low input power (such as 150 mW), we found that, for both the LBO and BBO crystal, the distance between the input lens and the crystal must be increased at higher powers to maintain optimal output, which means that the optimal beam waist position moves to the input end of the crystal at higher powers. This is consistent with the results in the previous section (Fig. 7). The shift of the optimal beam waist position is only an issue beyond 600-mW input power in our case and can be ignored otherwise (the optimal beam waist position remains unchanged). Experimentally this phenomenon is more serious when the input lens has a longer focal length (larger beam size in crystal), which indicates that it may have some dependence on the confocal parameter of the Gaussian beam in the crystal. Also, this effect is more serious for BBO than for LBO, which could be related either to the fact that the LBO crystal is longer or to its different material properties. For 8-mm BBO with a 140-mm input lens (the longest input focal length we used in the experiments), the distance between

the lens and the crystal has to be increased by 4.8 mm ( $0.38b_x$ ) to achieve optimal efficiency under 900-mW input power compared to the optimum distance at low input power. From what we showed previously, under low input powers, the optimal  $X$  beam waist satisfies  $f_0 = -0.22$  for a 140-mm lens. Based on the data in Table I (note that the “ $b$ ” values in crystals should be multiplied by  $n = 1.66$ ), the  $X$  beam waist is 1.4 mm away from the crystal center when it is optimized under low powers. This means that the optimal beam waist position at 900 mW could be 3.4 mm away from the crystal center and only 0.6 mm away from the input end of the crystal. For LBO, this phenomenon was only obvious with the 100- and 140-mm lenses and  $> 700$  mW input power. With the 140-mm input lens, the optimal position of the input lens at 900 mW input power has a 4.5-mm ( $0.37b_x$ ) difference from that at low input powers.

In the following experiments, at high input powers ( $\geq 700$  mW), we always adjusted the distance between the lens and the crystal to keep optimal output. Thus, from now on, our data points always represent the experimentally optimized output power with a certain lens at a certain input power.

Fig. 10 shows the optimal efficiencies for BBO with different input lenses at fixed input powers. The solid curves are calculated using (35); the dashed curves are calculated using (36) (the

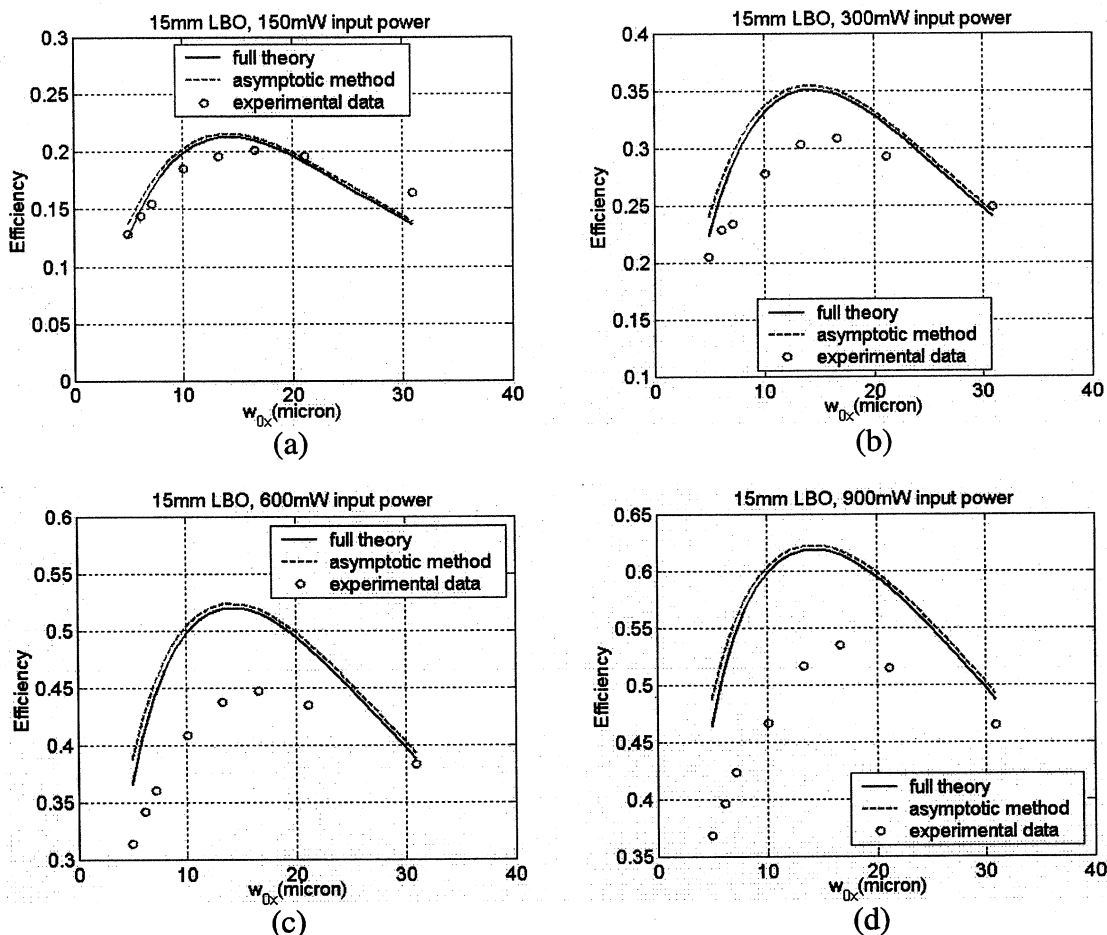


Fig. 11. The focusing dependence of optimal efficiency for LBO, similar to Fig. 10.

asymptotic method). The little circles are the data points. As we can see, the shape of the data points and our theoretical curves are very close under low input power (low pump depletion). The discrepancies increase as the input power increases, which is expected due to the nonlinear reshaping of the pump field. We can also notice the resemblance between Figs. 10 and 4, when SHG evolves from the nondepletion region to the depletion region. In Fig. 10, for the input powers of 150, 300, 600, and 900 mW, the pulse energies are 1.9, 3.8, 7.5, and 11.3 nJ, respectively. The difference between Figs. 10 and 4 is that in Fig. 4 the beam waist position is fixed, but in Fig. 10(d) the beam waist positions were adjusted to give experimentally optimized efficiency. The best efficiency we achieved with BBO was a little over 60% with an 80-mm input lens and 900-mW (maximum) input power.

Fig. 11 shows the focusing dependence for LBO crystal. Again we can see that the shape of the data points and the theoretical curves are very close under low input power. We can also see the resemblance between Figs. 11 and 5. The comments in the previous paragraph also apply here. The best efficiency we achieved with LBO was 54% with the 80-mm input lens at 900-mW input power.

In Figs. 10 and 11, it is also worth mentioning that the asymptotic method actually gives results very close to those of the double-integral method. The asymptotic method was derived based on the assumption  $l_{S-T} \ll b_x, b_y, L$ , so we expected it to

work just as well as the full theory with relatively loose focusing ( $b_x$  and  $b_y \gg l_{S-T}$ ) and sufficiently long crystals ( $L \gg l_{S-T}$ ). In Fig. 7(a) and (b), the asymptotic method deviates from the full theory more than in Figs. 4 and 5 because one of the assumptions  $L \gg l_{S-T}$  for the asymptotic method is no longer well satisfied when  $L$  is only 1 mm ( $L/l_{S-T}$  ranges from 2.7 to 8 in Fig. 7(a) and (b), while in Figs. 4 and 5 those numbers should be multiplied by 8). However, the  $l_{S-T} \ll b$  assumption seems to be less strict. In Fig. 10,  $b_x/l_{S-T}$  ranges from 4 (25-mm input lens) to 32 (140-mm input lens); in Fig. 11,  $b_x/l_{S-T}$  ranges from 0.9 (25-mm input lens) to 13 (140-mm input lens). Even though the  $l_{S-T} \ll b$  assumption is no longer well satisfied for the short focal-length lenses, the asymptotic method still seems to be quite close to the double-integral method in that region. It gives almost the same results as those of the double-integral method for BBO in Fig. 10, and only has a small deviation for LBO with short focal-length input lenses in Fig. 11. Considering that it is much easier to calculate, the asymptotic method could be a better way to estimate type-I SHG efficiency in many cases.

Fig. 12 shows the power dependence of the optimal SHG efficiency for both crystals with the 80-mm input lens (the lens which gives the highest efficiency). The solid curves are calculated from the double-integral method. The little circles are the data points. We did not show the results of the asymptotic method this time because they would be almost

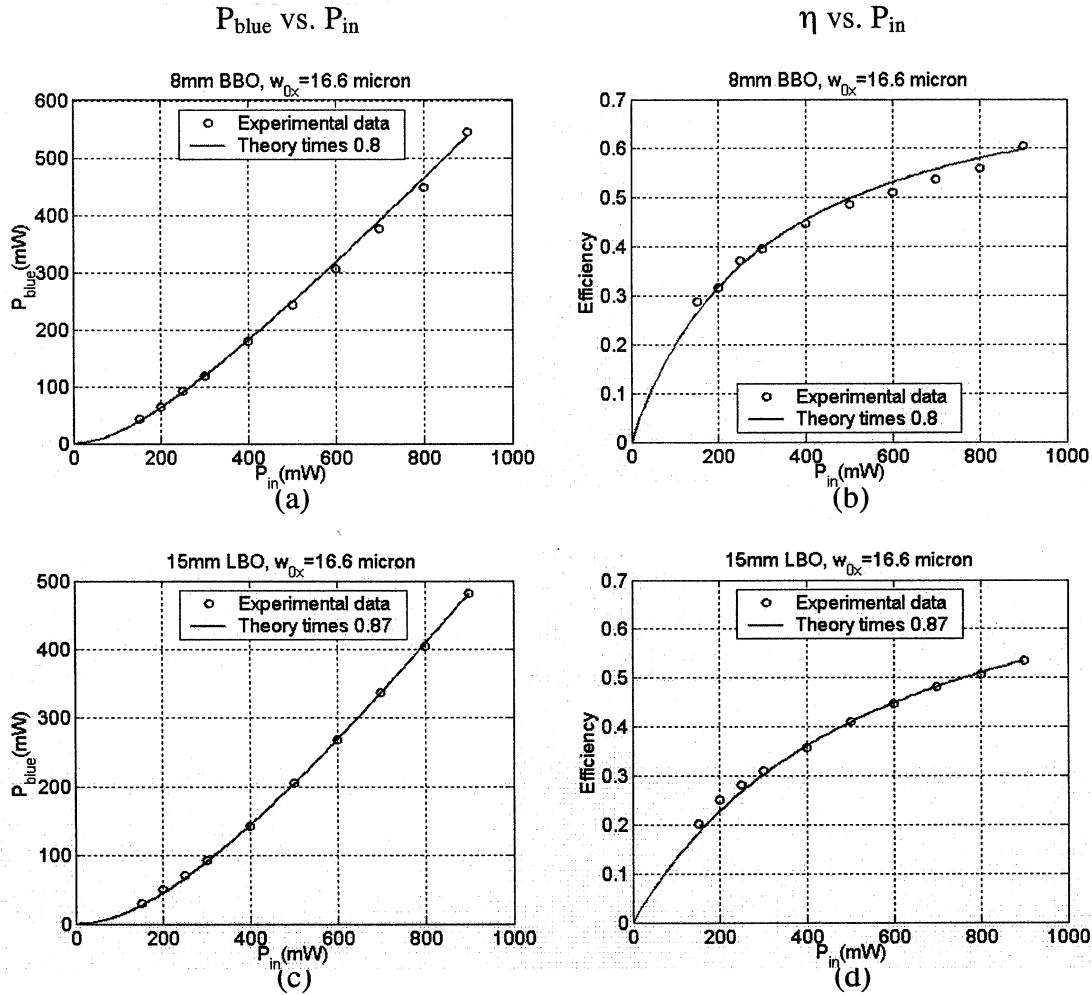


Fig. 12. The power dependence of optimal SH (blue) output and efficiency with 80-mm input lens. (a), (c) Optimal blue output power versus input power. (b), (d) Optimal efficiency versus input power. (a), (b) BBO. (c), (d) LBO. All theoretical results are multiplied by a factor as shown in figures.

identical to those of the double-integral method. Fig. 12(a) and (c) show the dependence of the optimal blue power versus input power, and Fig. 12(b) and (d) show the optimal efficiency versus input power. We multiplied the theoretical results by a numerical factor to fit the data, and we can see that the power dependences of the optimal blue power and efficiency do seem to follow a similar scaling rule in the depletion region as our theory indicated. Furthermore, there is no sign of a rollover with increasing power. This is in contrast to Fig. 9, where the crystal position was only optimized at low input powers.

## VII. CONCLUSION

We have developed a novel theory which for the first time can give the efficiency of type-I SHG with simultaneous temporal walk-off, spatial walk-off, and pump depletion in an analytical form. Within the nondepleted pump approximation, our theory may be considered as a generalization of [7], which is a well-known treatment of SHG with CW focused Gaussian beams, to include both space and time coordinates simultaneously. We further show how to extend into the depleted pump

regime, within the approximation that the pump spatial and temporal profile remains unchanged. We have compared the results of our theoretical model and those of a numerical solver (SNLO) and found that our theory and SNLO fit perfectly in the non-depletion region, but have discrepancies in the deep depletion region when the efficiency is well over 50%, because our treatment in the depletion region made the assumption of ignoring the nonlinear reshaping of the pump field due to depletion. We also performed experiments with two long SHG crystals (8-mm BBO and 15-mm LBO) and a 120-fs laser source. In the experiments, both spatial and temporal walk-off and pump depletion are important. The data generally support our theoretical results, especially for weak pump depletion. In the deep depletion region, we see discrepancies similar to what we saw in the comparison with SNLO, which can also be explained by the nonlinear reshaping. The experimental power dependence of the optimal efficiencies in the depletion region seems to follow a similar scaling rule, as predicted by our theory. Our theory provides an effective tool to predict the type-I SHG efficiency under many conditions not previously described via an analytical formulation and improves our understanding of the SHG conversion process itself.

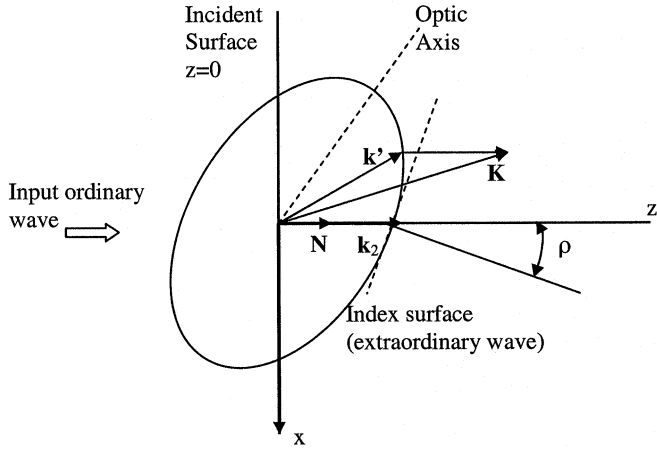


Fig. 13. The index surface and the vector mismatch relation in ooe type I SHG theory.

#### APPENDIX

In this appendix, we derive the integral expression for the harmonic field, (11). First we review some results from [4]–[6] for CW sources and ooe type-I SHG. We then show how to extend to the case of pulse sources. We will use the same notation here as in [4]–[7], i.e., Gaussian units and  $e^{-i\omega t}$  convention. To fit the results here to the equations in Section II, at the end of the Appendix we will need to convert from Gaussian units to MKS units and make a complex conjugate transformation in order to switch to the  $e^{+i\omega t}$  convention.

The SHG theory is based upon the inhomogeneous vector wave equation (in Gaussian units)

$$\nabla \times \nabla \times \vec{E}_2(\vec{r}, \omega) - \left(\frac{\omega}{c}\right)^2 \vec{\varepsilon}_2 \bullet \vec{E}_2(\vec{r}, \omega) = 4\pi \left(\frac{\omega}{c}\right)^2 \vec{P}_{NL}(\vec{K}, \omega) e^{i\vec{K} \bullet \vec{r}} \quad (39)$$

where  $\vec{\varepsilon}_2$  is the dielectric constant tensor at frequency  $\omega$ . The subscript 2 means SH field.  $\vec{P}_{NL}(\vec{K}, \omega)$  is the complex amplitude of the nonlinear plane-wave polarization field at frequency  $\omega$  and with an arbitrary wavevector  $\vec{K}$ . The solution of (39) consists of a forced wave and suitable free waves. The free waves are chosen to satisfy the boundary conditions of the problem, which in our case is that there is no SH field at the incident plane of the crystal.

In Fig. 13, the elliptical index surface [4] is for the SH wave (e wave). The wavevector of the fundamental wave and harmonic wave ( $\mathbf{k}_1$  and  $\mathbf{k}_2$ ) are both along the  $z$  axis, and  $\mathbf{N}$  is the unit vector along  $z$ . The walk-off angle  $\rho$  is the angle between the  $z$  axis and the normal to the index surface.  $\vec{K}'$  is a vector on the index surface such that  $\vec{K} - \vec{K}'$  is parallel to the  $z$  axis. [4] shows that, without absorption, under nearly matching conditions the growing wave is given by

$$\vec{E}_2(\vec{r}) = z \cdot g(2i\psi_K) \vec{\gamma} \bullet \vec{P}_{NL}(\vec{K}) e^{i\vec{K} \bullet \vec{r}} \quad (40)$$

where

$$\vec{\gamma} = 2\pi i \left(\frac{\omega}{cn}\right) \vec{U} \vec{U} \quad (41)$$

$$2\psi_K = (\vec{K} - \vec{k}') \bullet \vec{N} z \quad (42)$$

$$g(x) = \frac{(1 - e^{-x})}{x} = \int_0^1 e^{-xp} dp. \quad (43)$$

Here  $\mathbf{U}$  is a unit vector giving the polarization direction of the extraordinary harmonic wave, and  $n$  is the matched index. In our experiments,  $k_2 L$  is over  $10^4$ , so a nearly matching condition can still be applied when  $\Delta k L$  reaches 100. In (42), we need the  $z$  component of  $\vec{K} - \vec{K}'$ . To the second-order terms of  $K_x$  and  $K_y$ , we have [5]

$$2\psi_K = \left( K_z - k_2 + \rho K_x + \frac{K_x^2 + K_y^2}{2k_2} \right) z. \quad (44)$$

Generally the nonlinear polarization field is not plane-wave, and we will use Fourier transformation to get an integral result of

$$\vec{P}_{NL}(\vec{K}) = (2\pi)^{-3} \int \vec{P}_{NL}(\vec{r}') e^{-i\vec{K} \bullet \vec{r}'} d\vec{r}' \quad (45)$$

$$\vec{E}_2(\vec{r}) = z \int g(2i\psi_K) \vec{\gamma} \bullet \vec{P}_{NL}(\vec{K}) e^{i\vec{K} \bullet \vec{r}} d\vec{K}. \quad (46)$$

We can substitute (45) into (46) and exchange the order of integration. Then we can get an equation in the form

$$\vec{E}_2(\vec{r}) = \int \vec{\gamma} \bullet \vec{P}_{NL}(\vec{r}') G(\vec{r}, \vec{r}') d\vec{r}'. \quad (47)$$

$\vec{r}'$  represents the source point, and  $\vec{r}$  represents the observer point.  $G$  is called the interior Green's function (since it works when the observer point is inside the crystal). Without absorption the result is [6]

$$G_\omega(\vec{r}, \vec{r}') = \frac{1}{2\pi i} \frac{k_2}{Z} e^{ik_2(Z + (X^2 + Y^2)/2Z)}. \quad (48)$$

We added the subscript  $\omega$  since  $k_2$  is a function of  $\omega$ . In (48)

$$X = x - x' - \rho(z - z') \quad (49a)$$

$$Y = y - y' \quad (49b)$$

$$Z = z - z' \geq 0. \quad (49c)$$

As [6] shows, the important region is  $X^2 + Y^2 \ll Z^2$ . All parts of the wavelet which are not in this region destructively interfere and produce no resultant field. Thus, all the energy radiated at the source point flows along the direction of the Poynting vector. In this region, we have

$$R = Z + \frac{X^2 + Y^2}{2Z} \approx \sqrt{X^2 + Y^2 + Z^2}. \quad (50)$$

Now let us consider the pulsed source case, which is a new contribution of our paper. We need to expand the above theory by letting  $\vec{P}_{NL}$  have a distribution with respect to  $\omega$  as

$$\vec{P}_{NL}(\vec{K}, \omega) = (2\pi)^{-4} \int \vec{P}_{NL}(\vec{r}', t') e^{-i\vec{K} \bullet \vec{r}'} e^{i\omega t'} d\vec{r}' dt' \quad (51)$$

$$\vec{E}_2(\vec{r}, t) = z \int g(2i\psi_K) \vec{\gamma} \bullet \vec{P}_{NL}(\vec{K}, \omega) e^{i\vec{K} \bullet \vec{r}} e^{-i\omega t} d\vec{K} d\omega. \quad (52)$$

The source points will be  $(\vec{r}', t')$ , and the observer points will be  $(\vec{r}, t)$ . The definition of the Green's function then is

$$\vec{E}_2(\vec{r}, t) = \int \overleftarrow{\gamma} \bullet \vec{P}_{\text{NL}}(\vec{r}', t') G(\vec{r}, \vec{r}', t, t') \vec{r}' dt'. \quad (53)$$

Using (45)–(47) and (51)–(53), one can easily derive

$$G(\vec{r}, \vec{r}', t, t') = \frac{1}{2\pi} \int G_\omega(\vec{r}, \vec{r}') e^{-i\omega(t-t')} d\omega. \quad (54)$$

Using (48) and (54), we can derive the interior Green's function in the pulsed case as

$$G(\vec{r}, \vec{r}', t, t') = \frac{1}{(2\pi)^2 i} \int \frac{k_2}{Z} e^{ik_2(Z+(X^2+Y^2)/2Z)} e^{-i\omega(t-t')} d\omega. \quad (55)$$

We will need the following relationships in the calculation:

$$k_2 = k_{20} + \frac{\partial k_2}{\partial \omega} (\omega - \omega_2) = k_{20} + \frac{1}{V_2} (\omega - \omega_2) \quad (56)$$

$$\int e^{-i\omega t} d\omega = 2\pi \delta(t) \quad (57)$$

$$\int \omega e^{-i\omega t} d\omega = 2\pi i \delta'(t) \quad (58)$$

where  $V_2$  is the group velocity defined in (7), and  $\omega_2$  is the center frequency of the harmonic wave. The result of the calculation is

$$G(\vec{r}, \vec{r}', t, t') = \frac{1}{2\pi i} \frac{1}{Z} e^{ik_{20}R} e^{-i\omega_2(t-t')} \cdot \left[ k_{20} \delta\left(t-t' - \frac{R}{V_2}\right) + \frac{i}{V_2} \delta'\left(t-t' - \frac{R}{V_2}\right) \right]. \quad (59)$$

When the input is a pulsed Gaussian beam, the nonlinear polarization field is

$$\vec{P}_{\text{NL}}(\vec{r}', t') = \vec{P}_0 \frac{e^{2ik_1 z'} e^{-i\omega_2 t'}}{(1+i\tau_x(z'))(1+i\tau_y(z'))} \cdot \exp\left(-\frac{2x'^2}{w_{0x}^2(1+i\tau_x(z'))}\right) \cdot \exp\left(-\frac{2y'^2}{w_{0y}^2(1+i\tau_y(z'))}\right) f(t'). \quad (60)$$

Some explanations of the parameters in the above equation can be found below (8).  $f(t')$  represents the temporal complex amplitude, which is also Gaussian in our theory

$$f(t') = \exp\left(-\frac{4\ln 2\alpha' \left(t' - \frac{z'}{V_1}\right)^2}{t_p^2}\right) \quad (61)$$

where  $\alpha' = 1 - i\alpha/4$  (the minus sign is due to the  $e^{-i\omega t}$  convention), and  $\alpha$  is the same as in (8).  $\alpha$  will not be much bigger

than 1 unless the pulse is severely chirped. We can then substitute (59) and (60) into (53) to yield

$$\begin{aligned} \vec{E}_2(\vec{r}, t) &= \frac{\overleftarrow{\gamma}}{\gamma} \bullet \vec{P}_0 \frac{k_{20}}{2\pi i} e^{ik_{20}z} e^{-i\omega_2 t} \int_0^z \frac{e^{-i\Delta k z'}}{Z(1+i\tau_x(z'))(1+i\tau_y(z'))} dz' \\ &\cdot \iint dx' dy' \\ &\cdot e^{-2x'^2/w_{0x}^2(1+i\tau_x(z')) - 2y'^2/w_{0y}^2(1+i\tau_y(z')) + i(k_{20}(X^2+Y^2)/2Z)} \\ &\cdot \left[ f\left(t - \frac{R}{V_2}\right) + \frac{i}{k_{20}V_2} f'\left(t - \frac{R}{V_2}\right) \right]. \quad (62) \end{aligned}$$

Note that  $R$  is a function of  $x'$ ,  $y'$ , and  $z'$ . There are two facts that we can use to simplify the above equation. Using (61) we can write down the last bracket of (62) as follows:

$$\begin{aligned} f\left(t - \frac{R}{V_2}\right) + \frac{i}{k_{20}V_2} f'\left(t - \frac{R}{V_2}\right) \\ = e^{-(4\ln 2\alpha' (t-R/V_2-z'/V_1)^2)/t_p^2} \left[ 1 - \frac{i8\ln 2\alpha'}{k_{20}V_2 t_p^2} \left(t - \frac{R}{V_2} - \frac{z'}{V_1}\right) \right]. \quad (63) \end{aligned}$$

Temporally the important region is  $|t - R/V_2 - z'/V_1| < |3t_p/\sqrt{4\ln 2\alpha'}|$ . Outside this region the exponential term becomes very small and the contribution to the integral is negligible. In this important region, we claim that

$$\left| \left( \frac{8\ln 2\alpha'}{k_{20}V_2 t_p^2} \right) \left( t - \frac{R}{V_2} - \frac{z'}{V_1} \right) \right| < \left( \frac{12\sqrt{\alpha' \ln 2}}{k_{20}V_2 t_p} \right) \ll 1.$$

For our experiments,  $|\sqrt{\alpha'}| \approx 1.02$ ,  $k_{20}^{-1} \approx 40$  nm,  $V_2^{-1} \approx 5000$  fs/mm,  $t_p \approx 100$  fs, and calculation shows that  $|12\sqrt{\alpha' \ln 2}/k_{20}V_2 t_p| \approx 0.02 \ll 1$ . This means that the imaginary part in the bracket of (63) can be practically ignored, and so the same with the  $f'(t - R/V_2)$  term in (62). This approximation is more accurate with longer input pulses (larger  $t_p$ ) and may not be a good approximation for pulses as short as 10 fs.

Also, from (48) and (62), it is clear that  $R/V_2$  describes the time needed for the wave packet to travel from the source point to the observer point. From (49),  $X$  and  $Y$  describe the deviation of the wave packet propagation direction from the Poynting vector. As we mentioned above, spatially the important region is  $X^2 + Y^2 \ll Z^2$ , which means that the wave packets propagate very closely to the Poynting vector direction. All wave packets propagating outside this region destructively interfere and give no contribution. In the important region we make the approximation that when calculating the traveling time of wave packets, we assume that energy propagates strictly along the direction of the Poynting vector. Mathematically it means that we use  $R \approx Z$  and  $f(t - R/V_2) \approx f(t - Z/V_2)$ . With these approximations the temporal part in the integral of (62) is de-coupled from  $x'$  and  $y'$ .

$$\vec{E}_2(\vec{r}, t) = \vec{\gamma} \bullet \vec{P}_0 \frac{e^{ik_{20}z} e^{-i\omega_2 t}}{\sqrt{(1+i\tau_x(z))(1+i\tau_y(z))}} e^{-2y^2/w_{0y}^2(1+i\tau_y(z))} \int_0^z \frac{e^{-i\Delta kz'} e^{-2(x-\rho Z)^2/w_{0x}^2(1+i\tau_x(z))} f\left(t - \frac{z}{v_2} + \beta z'\right)}{\sqrt{(1+i\tau_x(z'))(1+i\tau_y(z'))}} dz' \quad (65)$$

$$A_2(x, y, L, t) = -i \frac{\omega_2 d_{\text{eff}}}{2n_2 c} \frac{A_0^2}{\sqrt{(1-i\tau_x(L))(1-i\tau_y(L))}} \exp\left(-\frac{2y^2}{w_{0y}^2(1-i\tau_y(L))}\right) \int_0^L \frac{\exp(i\Delta kz') \exp\left(-\frac{2(x-\rho L+\rho z')^2}{w_{0x}^2(1-i\tau_x(L))}\right) \exp\left(-\frac{\ln 2(4+i\alpha)\left(t - \frac{L}{v_2} + \beta z'\right)^2}{t_p^2}\right)}{\sqrt{(1-i\tau_x(z'))(1-i\tau_y(z'))}} dz' \quad (66)$$

We then can calculate the integral over  $x'$  and  $y'$  in (62) using the following formula [21]:

$$\int_{-\infty}^{+\infty} e^{-iax-ibx^2} dx = \left(\frac{\pi}{ib}\right)^{1/2} e^{ia^2/4b}, \quad \text{Im}(b) < 0. \quad (64)$$

The result is given in (65), shown at the top of the page.

To convert (65) to MKS units, first we need to do a complex conjugate transformation and set  $z = L$ . Note that  $\vec{E}_2(\vec{r}, t)$  here is equivalent to  $A_2(x', y', z', t') e^{i(\omega_2 t' - k_2 z')}$  in (1b), and  $\vec{U} \bullet \vec{P}_0$  here is  $\varepsilon_0 d_{\text{eff}} A_0^2$  from (2b). In MKS units, the  $4\pi/c^2$  in  $\vec{\gamma}$  ((41)) should be replaced by  $\mu_0$  [22]. After the conversion we will then have (66), shown at the top of the page. We can see that it is exactly the same as (11), which is the basis of the derivation of the SHG efficiency.

#### ACKNOWLEDGMENT

The authors would like to thank the reviewers for their very helpful comments, including the suggestion to compare our theory with SNLO.

#### REFERENCES

- [1] P. A. Franken, A. E. Hill, C. W. Peters, and G. Weinreich, "Generation of optical harmonics," *Phys. Rev. Lett.*, vol. 7, p. 118, 1961.
- [2] E. P. Ippen and C. V. Shank, *Ultrashort Light Pulses*, 2nd ed. Berlin, Germany: Springer, 1984, pp. 90–92.
- [3] R. Trebino and D. J. Kane, "Using phase retrieval to measure the intensity and phase of ultrashort pulses: Frequency-resolved optical gating," *J. Opt. Soc. Amer. A*, vol. 10, pp. 1101–1111, 1993.
- [4] D. A. Kleinman, "Theory of second harmonic generation of light," *Phys. Rev.*, vol. 128, p. 1761, 1962.
- [5] G. D. Boyd, A. Ashkin, J. M. Dziedzic, and D. A. Kleinman, "Second-harmonic generation of light with double refraction," *Phys. Rev. A*, vol. 137, p. 1305, 1965.
- [6] D. A. Kleinman, A. Ashkin, and G. D. Boyd, "Second-harmonic generation of light by focused laser beams," *Phys. Rev.*, vol. 145, p. 338, 1966.
- [7] G. D. Boyd and D. A. Kleinman, "Parametric interaction of focused gaussian light beams," *J. Appl. Phys.*, vol. 39, no. 8, p. 3597, 1968.
- [8] S. A. Akhmanov, A. P. Sukhorukov, and A. S. Chirkin, "Nonstationary phenomena and space-time analogy in nonlinear optics," *Sov. Phys. JETP*, vol. 28, p. 748, 1968.
- [9] R. C. Miller, "Second harmonic generation with a broadband optical maser," *Phys. Lett. A*, vol. 26, p. 177, 1968.
- [10] J. Comly and E. Garmire, "Second harmonic generation from short pulses," *Appl. Phys. Lett.*, vol. 12, p. 7, 1968.
- [11] W. H. Glenn, "Second-harmonic generation by picosecond optical pulses," *IEEE J. Quantum Electron.*, vol. QE-5, p. 284, 1969.
- [12] A. M. Weiner, "Effect of group-velocity mismatch on the measurement of ultrashort optical pulses via 2nd harmonic-generation," *IEEE J. Quantum Electron.*, vol. 19, pp. 1276–1283, Aug. 1983.
- [13] G. Imeshev, M. A. Arbore, S. Kasriel, and M. M. Fejer, "Pulse shaping and compression by second-harmonic generation with quasiphase-matching gratings in the presence of arbitrary dispersion," *J. Opt. Soc. Amer. B*, vol. 17, no. 8, pp. 1420–1437, 2000.
- [14] A. M. Weiner, A. M. Kan'an, and D. E. Leaird, "High efficiency blue generation by frequency doubling of femtosecond pulses in a thick nonlinear crystal," *Opt. Lett.*, vol. 23, no. 18, pp. 1441–1443, 1998.
- [15] A. V. Smith, R. J. Gehr, and M. S. Bowers, "Numerical models of broadband nanosecond optical parametric oscillators," *J. Opt. Soc. Amer. B*, vol. 16, no. 4, pp. 609–619, 1999.
- [16] [Online]. Available: [www.sandia.gov/imrl/XWEB1128/xxtal.htm](http://www.sandia.gov/imrl/XWEB1128/xxtal.htm)
- [17] J. A. Arnaud and H. Kogelnik, "Gaussian light beams with general astigmatism," *Appl. Opt.*, vol. 8, p. 1687, 1969.
- [18] D. A. Roberts, "Simplified characterization of uniaxial and biaxial nonlinear optical crystals – A plea for standardization of nomenclature and conventions," *IEEE J. Quantum Electron.*, vol. 28, pp. 2057–2074, Oct. 1992.
- [19] K. Kato, "Second-harmonic generation to 2048 Å in  $\beta$ -BaB<sub>2</sub>O<sub>4</sub>," *IEEE J. Quantum Electron.*, vol. QE-22, pp. 1013–1014, July 1986.
- [20] —, "Tunable UV generation to 0.2325- $\mu$ m in LiB<sub>3</sub>O<sub>5</sub>," *IEEE J. Quantum Electron.*, vol. 26, pp. 1173–1175, July 1990.
- [21] I. S. Gradshteyn and I. M. Ryzhik, *Table of Integrals, Series, and Products*, 5th ed. New York: Academic, 1996.
- [22] S. Ramo, J. R. Whinnery, and T. V. Duzer, *Fields and Waves in Communication Electronics*, 3rd ed. New York: Wiley, 1993, p. 814.

**Haifeng Wang** was born in Wuhan, China, in 1975. He received the B.S. degree in electronic engineering from Tsinghua University, Beijing, China, in 1998. He is currently working toward the Ph.D. degree in electrical and computer engineering at Purdue University, West Lafayette, IN.

He has published previous work on optical pulse shapers. His main areas of research interest include optical pulse shaping and nonlinear optics.

**Andrew M. Weiner** (S'84–M'84–SM'91–F'95) received the Sc.D. degree in electrical engineering from the Massachusetts Institute of Technology (MIT), Cambridge, in 1984.

From 1979 through 1984, he was a Fannie and John Hertz Foundation Graduate Fellow at MIT. In 1984, he joined Bellcore, at that time one of the premier research organizations in the telecommunications industry. In 1989, he was promoted to Manager of Ultrafast Optics and Optical Signal Processing. He moved to Purdue University, West Lafayette, IN, in 1992 as Professor of Electrical and Computer Engineering. He is currently the Scifres Distinguished Professor of Electrical and Computer Engineering as well as ECE Director of Graduate Admissions. His research focuses on ultrafast optical signal processing and high-speed optical communications. He is especially well known for pioneering the field of femtosecond pulse shaping, which enables generation of nearly arbitrary ultrafast optical waveforms according to user specification. He has published four book chapters and over 120 journal articles. He has been author or coauthor of over 200 conference papers, including approximately 60 conference-invited talks, and has presented over 50 additional invited seminars at universities or industry. He holds 5 U.S. patents.

Prof. Weiner has received numerous awards for his research, including the Hertz Foundation Doctoral Thesis Prize (1984), the Adolph Lomb Medal of the

Optical Society of America (1990), awarded for pioneering contributions to the field of optics made before the age of thirty, the Curtis McGraw Research Award of the American Society of Engineering Education (1997), the International Commission on Optics Prize (1997), the IEEE LEOS William Streifer Scientific Achievement Award (1999), the Alexander von Humboldt Foundation Research Award for Senior U.S. Scientists (2000), and the inaugural Research Excellence Award from the Schools of Engineering at Purdue (2003). He is a Fellow of the Optical Society of America. He has served on or chaired numerous research review panels, professional society award committees, and conference program committees. In 1988–1989, he served as an IEEE Lasers and Electro-Optics Society (LEOS) Distinguished Lecturer. He was General Co-Chair of the 1998 Conference on Lasers and Electro-optics, Chair of the 1999 Gordon Conference on Nonlinear Optics and Lasers, and Program Co-chair of the 2002 International Conference on Ultrafast Phenomena. In addition, he has served as Associate Editor for IEEE JOURNAL OF QUANTUM ELECTRONICS, IEEE PHOTONICS TECHNOLOGY LETTERS, and *Optics Letters*. He served as an elected member of the Board of Governors of IEEE LEOS from 1997–1999 and as Secretary/Treasurer of IEEE LEOS from 2000 to 2002. He is currently a Vice-President (representing IEEE LEOS) of the International Commission on Optics (ICO).